Interface mobility between monomers in dimeric bovine ATP synthase participates in the ultrastructure of inner mitochondrial membranes

Tobias E. Spikes, Martin G. Montgomery and John E. Walker[1]

The Medical Research Council Mitochondrial Biology Unit, University of Cambridge, Cambridge Biomedical Campus, Hills Road, Cambridge CB2 0XY, United Kingdom

[1]To whom correspondence should be addressed. J. E. W., Tel.: +44-1223-252701; e-mail: walker@mrc-mbu.cam.ac.uk

Running title: ATP synthase mobility

The authors declare no conflict of interest

Author contributions: T. E. S. and J. E. W. designed research; J. E. W. supervised project; T. E. S. and M. G. M. performed research; T. E. S., M. G. M. and J. E. W. analyzed data; J. E. W., T. E. S. and M. G. M. wrote the text, T. E. S. and M. G. M. prepared the figures and T. E. S. made the movies.

Key words: bovine mitochondria; ATP synthase; dimer; monomer-monomer interface; mobility

Abstract

The ATP synthase complexes in mitochondria make the ATP required to sustain life by a rotary mechanism. Their membrane domains are embedded in the inner membranes of the organelle and they dimerize via interactions between their membrane domains. The dimers form extensive chains along the tips of the cristae with the two rows of monomeric catalytic domains extending into the mitochondrial matrix at an angle to each other. Disruption of the interface between dimers by mutation affects the morphology of the cristae severely. By analysis of particles of purified dimeric bovine ATP synthase by cryo-electron microscopy, we have shown that the angle between the central rotatory axes of the monomeric complexes varies between *ca.* 76-95°. These particles represent active dimeric ATP synthase. Some angular variations arise directly from the catalytic mechanism of the enzyme, and others are independent of catalysis. The monomer-monomer interaction is mediated mainly by j-subunits attached to the surface of wedge-shaped protein-lipid structures in the membrane domain of the complex, and the angular variation arises from rotational and translational changes in this interaction, and combinations of both. The structures also suggest how the dimeric ATP synthases might be interacting with each other to form the characteristic rows along the tips of the cristae via other inter-wedge contacts, moulding themselves to the range of oligomeric arrangements observed by tomography of mitochondrial membranes, and at the same time allowing the ATP synthase to operate under the range of physiological conditions that influence the structure of the cristae. [248 words]

Significance (120 words)

Mitochondria are the power houses of eukaryotic cells. Pairs of molecular machines with a rotary action, called ATP synthase, are embedded in their inner membranes and produce adenosine triphosphate, ATP, the fuel of life. These dimers form long rows on cristae tips, helping to endow them with their characteristic and mobile tubular shape. Our structural analyses of bovine dimers show that some structural changes depend on catalysis, and others are independent. The monomers pivot and translate at wedge shaped structures in their membrane domains. The structures suggest how dimeric ATP synthases might interact and fashion themselves to the range of oligomeric arrangements observed in mitochondria, whilst allowing the ATP synthase to produce ATP under a wide range of physiological conditions. [120 words]

INTRODUCTION

The ATP synthase complexes embedded in the inner membranes of mitochondria (IMM) are rotary machines that make the ATP required to sustain life (1). Energy from respiration generates a proton motive force (pmf) across the IMM, and this pmf is applied directly to the membrane embedded sector of the rotor of the ATP synthase via a Grotthuss chain of water molecules, thereby generating rotational torque to turn the rotor in the synthetic direction of rotation (2). In mammals, this membrane sector of the rotor is composed of a ring of eight c-subunits, and is attached to an extramembranous central stalk assembly of subunits γ, δ and ε, which penetrates into the extramembranous $\alpha_3\beta_3$-catalytic domain *ca.* 90 Å distant from the membrane domain (2, 3). Three of the six interfaces between α- and β-subunits contain the catalytic sites of the enzyme, and as the rotor turns in 120° steps during the rotary cycle, these sites undergo a series of structural changes that are associated

in turn with the binding of substrates, and the formation and release of ATP from each site (4). The catalytic domain is also attached to the membrane domain via a peripheral stalk (PS), an elongated rod that reaches *ca.* 150 Å between the catalytic domain and the surface of the IMM (2, 5, 6). The core of the rod is provided by a long α-helix, bH3, which extends between the $\alpha_3\beta_3$-catalytic domain and the IMM, and then penetrates and crosses the IMM to reach the intermembrane space (IMS) and then returns to the mitochondrial matrix via a second transmembrane span. The membrane extrinsic part of bH3 is supported and largely rigidified by other α-helices in the d- and F_6-subunits and in the membrane extrinsic region of subunit ATP8, all bound approximately parallel to the membrane extrinsic region of bH3. The upper part of the rod is attached via the C-terminal α-helix of subunit b, bH4, to the C-terminal domain of the OSCP subunit, and the N-terminal domain of this subunit binds to the N-terminal regions of the three α-subunits. The two domains of the OSCP are joined by a flexible linker, which provides the PS with a universal joint. During the rotary catalytic cycle, the $\alpha_3\beta_3$-domain rocks from side to side, as noted before (7–10), with little or no displacement perpendicular to the lateral motion of the PS towards the central axis of the rotor (2), and the PS accommodates this rocking motion via the combined action of the universal joint, and a hinge in the PS close to the surface of the IMM (2). The membrane bound N-terminal region of the b-subunit is folded into two further α-helices, bH1and bH2, and together with the transmembrane domain of bH3, they form the skeleton of a wedge-shaped structure in the membrane domain (2), with bH1 sitting on top on the matrix side of the IMM and transmembrane α-helices bH2 and bH3 subtending an angle of *ca.* 45°. Supernumerary subunits e, f and g also contribute to the structure of the wedge. The transmembrane α-helices eH1 and gH3 of subunits e and g augment α-helix bH2, and the

top of the wedge on the matrix side of the membrane is provided by four amphipathic α-helices, two in each of the g- and f-subunits, lying in the lipid head-group region. Internal cavities in the wedge are occupied by five specifically bound lipids, three cardiolipins (CDL1, CDL2 and CDL3) and two less well defined phospholipids modelled tentatively as phosphatidyl glycerols (LHG4 and LHG5). These phospholipids enhance the stability of the wedge (2). Subunit j is associated with the wedge, and in the dimeric complex the two j-subunits interact with each other across the monomer-monomer interface. In the IMM of the mitochondria, the dimeric ATP synthase complexes occupy the tips of the cristae, and the dimers are arranged in long rows along the tips of the cristae (11–13). How the dimers are held together in higher oligomers is uncertain, but protein-protein interactions in the membrane domains of dimers may provide inter-dimer tethers (2, 14). If the capacity of the monomeric complexes to form dimers is removed, for example by deletion of one of the wedge components, the structure of the IMM changes dramatically, and the cristae tubes disappear (15–21). Thus, the dimerization of the ATP synthase appears to be a determinant of the formation of cristae. These dynamic ATP synthase complexes operate in the ever changing structural context of the mitochondria themselves. The organelles are constantly being re-modelled by fission of mitochondrial networks and by fusion of vesicular mitochondria, influenced, for example, by cellular conditions such as energetic state, the cell-cycle or by pro-apoptotic or cell-death factors (22). The fusion and fission events involve changes in both inner and outer membranes, in the latter case again influencing the structures of the cristae and the disposition of the dimeric ATP synthase complexes within them. During these dynamic events and under conditions of active cellular growth, the IMM needs to remain coupled to ATP synthesis. Therefore, in order to

remain active, the dimeric ATP synthase not only has to accommodate changes in the monomer-monomer interface that arise directly from its own catalytic activity, but also others that stem from the dynamics of the organelle itself, and without dissipating the pmf by leakage of protons through the monomer-monomer interface. In tomographic reconstructions of mitochondrial cristae, zig-zagging, lateral bending, perpendicular curvature and non-uniform packing of rows of dimers of ATP synthase have been observed (12, 17, 23), illustrating the wide range of varying modes of oligomerization under which the ATP synthase complexes operate.

As shown here, the interaction between the two wedges linking the monomers in the dimeric ATP synthase is not a constant feature. It changes to accommodate both the rocking motions of the membrane extrinsic catalytic domain associated with catalysis, and other motions that are independent of catalysis observed in the isolated dimeric ATP synthase. These pivoting motions and sliding translations between the monomeric complexes are intrinsic features of the dimeric ATP synthase. They allow it to operate in the ever-changing ultrastructure of the IMM and also to contribute to their ultrastructure.

Results and Discussion

Classification of dimeric particles of bovine ATP synthase

As described before, three data-sets of 4,267, 2,238 and 4,096 dose-fractionated exposures of the purified dimeric bovine ATP synthase were collected, and structures of the monomeric enzyme were produced by single particle analysis of 176,710 particle coordinates (2). Although each monomer is inhibited by a monomeric form of the inhibitor protein, IF_1, the inhibitor has trapped dimeric states where each monomeric catalytic domain contains the same three rotational points in the active catalytic cycle. The positions

of these three rotational points relative to the peripheral stalk gives rise to three states of the intact monomeric ATP synthase named s1, s2 and s3. Complete structures of the monomeric complex were built (2), and by combining states s1, s2 and s3 (see *SI Appendix*, Table S1), models of dimeric complexes were constructed in a range of combinations of catalytic states and sub-states (see *SI Appendix*, Scheme S1 and Table S2). The sub-states arise from changes that are independent of catalysis in the relative disposition of the two monomers to each other (see *SI Appendix*, Scheme S2). By hierarchical classification of the earlier data-set (*SI Appendix*, Scheme S1) and subsequent refinement, 154,130 particles were resolved into nine discrete classes of the dimeric assembly representing rotational states [s1:s1], [s1:s2], [s1:s3], [s2:s1], [s2:s2], [s2:s3], [s3:s1], [s3:s2], and [s3:s3] at resolutions of 9.2, 11.9, 9.0, 9.4, 8.5, 10.7, 9.7, 11.4 and 13.1 Å, respectively. Composite dimer models were created by rigid body fitting of the maps and associated atomic coordinates (2) into these lower resolution envelopes. Further classification of the particles in each catalytic state (*SI Appendix*, Scheme S2) revealed fifty-nine additional sub-states of the dimer, at resolutions ranging from 13.8-23.8 Å. The sub-states are distinguished from discrete classes of the dimeric assembly in defined rotational states by sequential lettering and are grouped according to catalytic state. For example, the first, second and third sub-states of the ATP synthase dimer in which the right and left monomers are in catalytic states 1 and 3, respectively, are referred to as dimer sub-states [s1:s3a], [s1:s3b] and [s1:s3c].

Changes in the monomer-monomer interface during catalysis

In the dimeric complex, the monomer:monomer interface in the membrane domain consists of contacts between the two j-subunits each on the external surface of the wedge (Fig. 1

and *SI Appendix*, Fig. S1 *A*). From residues 1-20, subunit j is folded into an amphipathic α-helix jH1, which lies in the lipid head group region on the matrix side of the IMM where it interacts with the C-terminal region of transmembrane α-helix A6LH1 and CDL1. The negatively charged headgroup of CDL1 is bound to jK8, and to residues fQ38 and fY42 of the f-subunit in the wedge and residues aT33, and A6LK27 and A6LK30 (see *SI Appendix,* Fig. S1 *B*). Transmembrane α-helix jH2 (with residues 22-39 forming the transmembrane span) lies adjacent to A6LH1 on the opposite side of aH1 to the wedge, and is associated with subunit a via interactions between its N-terminal region and residues 107-108, 110-111 and 114-115 of aH4 (see *SI Appendix*, Fig. S1 *A, B*). The C-terminal region of jH2 (residues 40-49), protrudes into the IMS. Residues j50-60 were not modelled as they were not well defined in the cryo-em reconstructions. They are predicted to have an extended structure (see *SI Appendix*, Fig. S2) that interacts with the same region in the adjacent j-subunit, as indicated by the structures of the dimers in various rotational states and many of their sub-states, where density beyond the modelled residues can be observed (see *SI Appendix*, Fig. S1 *D-F*). However, the interactions between the two j-subunits are mobile, and the observed angle between the central axes of the central stalk or the PS of the monomers ranges from *ca*. 75-86° in the nine rotational catalytic states (see *SI Appendix*, Movies S1 and S2). This range of angles arises by the rigid body of the wedge and the rest of the membrane domain pivoting about contact points between the amphipathic α-helices jH1 (residues 1-20), provided by residues 3, 7, 10, 11 and 14 (see Figs. 2 and 3, *SI Appendix* Fig. S1). The two jH1 α-helices are oriented in the plane of the IMM on the matrix side as the enzyme contorts during the rotational cycle (see Figs. 1 and 2, and *SI Appendix*, Movie S3). Residues 3, 7, 10, 11 and 14 in jH1 project toward the interface possibly interacting

via an intervening lipid. This pivoting reduces the net side-to-side displacement of the catalytic domain arising from the rotation of the asymmetrical central stalk, and accommodates other changes in the structure of the dynamic mitochondrial cristae.

Changes in the monomer-monomer interface unrelated to catalysis

Other variations in motion occurring within groups of particles of a defined catalytic state are sub-states that are independent of catalysis. They fall into two categories, namely those where the angle between rotatory axes is less than 90° (*SI Appendix*, Movie S4) and others where the angle is greater than 90° (*SI Appendix*, Movies S5 and S6). The motions in the former category are similar to those that occur during catalysis in that the relative dispositions of the membrane domains change by a pivoting motion about the interface between j-subunits, with the C-terminal IMS protrusions remaining in contact. The flexibility of this pivot is an intrinsic property of the interface and it has other roles beyond that described above of dissipating the rocking of the catalytic domain in the mitochondrial cristae. Most notably, it provides a mechanism to accommodate the general fluidity of the membrane in the region of curvature associated with the dimeric ATP synthases and the rearrangements that occur. The second category of motions between sub-states, where the angle between rotatory axes exceeds 90°, arises from sliding and twisting along the monomer-monomer interface presented by the a and j subunits and the membrane wedge, thereby effecting a compound rotation of one monomer relative to the other (see Fig. 4 and *SI Appendix*, Movies S4 and S5). For example, in Fig. 4, where the structures of the ATP synthase dimers in the sub-states [s2:s2c] and [s2:s2b] are compared, the positions of the protrusion of subunit j into the IMS and of the loop region (residues 12-19) in subunit a

differ significantly in the two structures (see *SI Appendix*, Movie S5 and S6). In sub-state [s2:s2c], the C-terminal residues of subunit j are in contact in the IMS as in Fig. 4*C*. In contrast, in sub-state [s2:s2b], these residues are displaced by *ca.* 20 Å and the two loops consisting of residues 12-19 of subunit a appear to make contact with each other, as in Fig. 4*D*. This compound rigid body rotation of the monomers changes the angle between the rotatory axes significantly, and also re-arranges the amphipathic α-helices lying in the IMS leaflet of the membrane (see Fig. 4 and *SI Appendix*, Movies S5 and S6). In the IMM, this transformation could be part of a mechanism for the dimers and oligomeric rows to adapt to the convolutions of the cristae, with the two contact positions representing a simple steric mechanism that restrains the rotation to upper and lower limits. In this mechanism, the wide angle conformation (as observed in sub-state [s2:s2b]; see Fig. 4*B*, *D* and *F*) rests at the position where the two a-subunits are in contact and is prevented from widening further by aH1, and the conformation with a shallow angle (for example, the sub-state [s2:s2c] in Fig. 4*A*, *C* and *E*) rests at the position where the two j-subunits are in contact in the IMS. There is probably a continuum of sub-states between the two extremes. The conformers with shallow angles between rotatory axes of *ca*. 76° to 86° were the most abundant observed sub-states (see *SI Appendix*, Fig. S3 and Scheme 2). The highly dynamic nature of the dimeric complex is demonstrated by the compilation of all the observed conformers in *SI Appendix*, Movie S7.

It cannot be excluded that the wide angle sub-states with rotatory axis angles greater than *ca.* 95°, which depart significantly from the consensus structures with rotatory axis angles of *ca.* 76-86°, arise from the influence of the detergent micelle and the lack of the interactions between dimers that occur in native membranes. In curved membranes, an

estimated tension of *ca* 10 mN/m is exerted on mechanosensitive channels (24, 25), and it is possible that force from mitochondrial lipids at the cristae apices stabilizes the dimer interface, and *in situ* this lateral force might reduce the range of motion observed in isolated monomers. The sub-tomographic reconstructions of dimeric ATP synthases from mammalian mitochondria, where rotatory axis angles of *ca.* 80° have been reported, represent the average structures of many individual molecules, or sub-tomograms, within the data (12), similar to the consensus dimer in *SI Appendix*, Scheme S1. Therefore, they do not exclude the possibility of large variations in the angle of the rotatory axis, especially if those conformations arise rarely, for example at cristae ultrastructures with sharp negative curvature, or during dynamic rearrangements of the cristae, and indeed the dimer sub-states with wider angles are relatively rare (see *SI Appendix*, Fig. S3*C* and *D* and Scheme S2). Although it is not certain whether these very wide rotatory axis angle substates occur in native membranes, as the analysis was performed on isolated dimers, the data strongly suggest that the interfaces between monomers are significantly dynamic and that this dynamism is a general property of the interface, linked to motions of the enzyme that are both dependent and independent of catalysis. Indeed this dynamism, which manifests as pseudo-c2 symmetry about the dimer interface, necessitated specific refinement strategies to prevent the rotation of particle orientations about the pseudo-c2-axis in order to isolate and subsequently maintain catalytically homogenous particle sub-sets during further particle-realignment (see *SI Appendix*, Scheme 1). Therefore, during image processing, each monomer was given the arbitrary designation “left or “right” with respect to a single viewing direction, and, for example, the state [s1:s2] and state [s2:s1] dimers are distinct and do not represent the same molecular state.

Interactions between dimers

The issue of how dimeric ATP synthases interact with each other in the long rows that form along the apices of the cristae in the IMM cannot be resolved definitively by the current study of the structure of the isolated bovine dimers. However, the structures and other information suggest how the dimeric ATP synthases might reasonably form tetramers and higher oligomers involving homo-interactions between the two copies of each of subunits g and k. In the dimeric bovine structure, the 102 amino acid residue g-subunit is folded into three α-helices, gH1 (residues 20-36), gH2 (residues 42-60) and gH3 (residues 69-93) with transmembranous gH3 augmenting the skeleton of wedge, and amphipathic gH1 and gH2 associated with the top of wedge on the matrix side of the IMM. In the dimeric complex, the two gH2s have the capability to contact each other across the dimer-dimer interface and link the dimers together, as depicted in Fig. 5, with weak interactions across the dimer-dimer interface between residues gQ50, gK53 and gK54 in each protomer (see Fig. 7) providing a potential molecular basis for the requisite sliding, translational and rotational elements to generate the wide range of cristae structures that have been observed in mitochondria. Such a fluid interface would allow, for example, the long rows of ATP synthase oligomers to follow the curvature along the apices of the cristae (see Fig. 5*B*-*D*), and to readjust their positions as the curvature changes, without impeding the dynamics of the cristae. This fluidity is illustrated in Fig. 5*B*, where the ATP synthase dimers follow the curvature of the IMM along the axis shown in Fig. 5*C* and 5*D*. The fluidity of the dimer-dimer interface could allow either a rotation about a fixed contact point between g-subunits, or dislocate the contact and translate the dimers sideways (see Fig. 6*A*). These adjustments of inter-dimer contacts, and combinations of them, can engender a range of oligomeric

arrangements which are inferred here from geometric considerations and from the presentation of ATP synthase dimers in tomographic reconstructions of mitochondrial cristae. They include non-uniform packing (Fig. 6*B*-*G*), where rotation about a fixed contact point produces lateral bends in oligomer rows (as viewed from above; see Fig. 6*F* and 6*G*), and where contact dislocation permits the dimers to stack in a compact arrangement (Fig. 6*C* and *E*), or to form staggered rows (Fig. 6*D*). These arrangements are constrained geometrically in the cristae by the spherical catalytic domains of the enzyme. Thinning of the footprint of the membrane domain of the dimer, as viewed from above or below the membrane, resulting from changes in the angle between the rotatory axes as described in Fig. 4 and in *SI Appendix*, Movies S5 and S6, places adjacent catalytic domains in closer proximity, and therefore limits the degree of lateral curvature of the oligomeric row. Such a mobile contact also accounts for the positive and negative curvature along the cristae rows (see Fig. 5*C* and *D*), and, in a variety of combinations with dislocations, produces zig-zagging, lateral bending, perpendicular curvature and non-uniform packing. The oligomer rows may also deform plastically, much like an armature wire in a sculpture model, providing strength to maintain the apex of the cristae over long distances, simultaneously allowing different types of ultrastructure, such as lateral and perpendicular bends, to form. Many of these arrangements have been observed in tomographic reconstructions of the cristae (12, 17, 23).

It is also possible that subunit k could be involved in linking dimers together. During the process of assembly of the closely related human enzyme, this subunit is the last to be incorporated into complex, and in human cells grown under glycolytic conditions, subunit k turned over more rapidly than the other subunits of the enzyme which turned over

together at a slower rate (26). These observations led to the suggestion that subunit k might participate in a mechanism for remodelling IMMs (26). The partial structure of bovine k is compatible with this proposal. In the dimeric bovine complex, residues 12-47 of the 57 residue subunit k were resolved (2). The N-terminal region of the k-subunit is folded into a short α-helix, kH1, from residues 14-17 and is linked to kH2 by a loop (residues 18-23). This region is followed by the single transmembrane α-helix, kH2, from residues 24-44 which is associated with subunit a via interactions with aH4 and aH5. The C-terminal region (residues 45-57) of subunit k is in the IMS and is predicted to be extended. Thus, it is possible that in the IMM, this extended region could be in contact with the C-terminal region of subunit g across the dimer-dimer interface. The distance between k and g subunits in adjacent dimers decreases as the angle between rotatory axes in the dimer increases. Rearrangement of wedge subunits along the dimer interface, concomitant with changes to the rotatory axes as shown in *SI Appendix*, Movies S5 and S6, narrows the membrane footprint of the dimer thereby bringing adjacent dimers closer.

Influence of the inhibitor protein IF_1

Another mode of interaction of two ATP synthase dimers has been described where two inactive dimers are linked into tetramers of porcine (14) and ovine (27) ATP synthases by two dimeric IF_1 molecules spanning between the globular F_1-domains across the interface between the two dimeric ATP synthases. However, the membrane domains of the porcine tetramer were mis-interpreted (2), but in a corrected structure (2), and in the structure of the ovine dimeric enzyme (27), the g-subunits from adjacent dimers are in contact on top of the matrix side of the membrane via gH2 and the preceding loop (residues 39-53), the membrane domains of the e-subunits are in close contact, and residues 13 and 14 of subunit

k interact with gH1 on the matrix side of the membrane (2). In addition, its unresolved C-terminus could interact with subunits g and a on the IMS side of the IMM. These tetrameric units require the catalytic states of the adjacent dimers to be [s1:s3] and [s3:s1] or *vice versa*.

The physiological relevance of this inactive tetramer is unclear. Both the porcine and ovine tetramers were purified from mitochondria isolated from animal hearts. Therefore, these experiments provide no information about whether the active dimers described here and these inactive tetramers co-exist within the same mitochondrion. The co-existence of active dimers and inactive dimers within the same mitochondrion can be envisaged in two instances. First, individual cristae within a mitochondrion can have different membrane potentials (28). Therefore, both ATP synthesis by active dimers, and ATP hydrolysis followed by inhibition by IF_1 and formation of tetramers could happen at the same time in different cristae in the same mitochondrion. Second, if the prevailing physiological conditions led to activated IF_1 dimers, but there was, despite its apparent abundance in mitochondria (29), insufficient active IF_1 to inhibit the hydrolytic action of the dimeric ATP synthases, then this situation could lead to a mixture of active ATP synthase dimers in hydrolytic mode, and inhibited dimers within tetramers.

Independent of these physiological considerations, the structures of free dimers and equivalent dimers in tetramers differ substantially, and, for example, the angle between the rotatory axes of monomers in each dimer in tetramers is 112-116° whereas it *is ca*. 76-95° in free dimers. This wider angle between monomers in dimers within tetramers is accompanied by an outward bending of each rotatory axis and a significant rearrangement of the interface between monomers in the dimers (the interface is compressed to allow

close association of the catalytic domains, which is otherwise sterically prohibited by the g-subunit). The membrane domain of the tetramer has undergone a structural re-arrangement where the individual monomeric membrane domains appear to have collapsed inwards: see the change in the inclination of the c_8-rings (*SI Appendix* Fig. S4). Also, the tethering of adjacent catalytic domains by IF_1 induces a torsion in the F_1 and PS domains, tilting the rotatory axes accompanied by narrowing of the membrane domain in the dimeric unit (*SI Appendix* Fig. S5). This change in the membrane domains could have arisen from the effects of extraction of the complexes from the membrane with detergents and the loss of endogenous lipids (*SI Appendix*, Fig. S4). Thus, it is possible that the binding of the two IF_1 dimers to form the ATP synthase tetramers occurs during this extraction procedure, and that the formation of tetramers is an artefact. Relaxation of the tilted geometry of adjacent dimers and the dimer-dimer interface in the porcine and ovine tetramers is not possible because of the close proximity of the catalytic domains and this prevents the formation of planar oligomeric rows. In contrast, the models of oligomerisation of active dimers proposed here permit the formation of the variety of oligomeric arrangements needed to produce the geometry of the IMM. Also, they are compatible with the fluidity of the dimer interface observed in the structures of the bovine dimers (see Fig. 4, and *SI Appendix* Movies S4-7). These models of oligomerisation of active dimers are incompatible with formation of inactive tetramers (*SI Appendix*, Fig. S6). The changes to the architecture of the membrane domains in the tetrameric structures produce a rigid curvature along the axis of oligomerisation that is incompatible with the ultrastructures of the IMM observed by tomography (12, 17, 23), and the tetrameric structures inhibit the fluidity in oligomeric rows observed *in vivo*. Thus, this conformation is unlikely to be relevant in consideration

of the wider plasticity of the IMM, especially as the *in silico* association of tetrameric complexes leads to a closed loop within six dimeric units (*SI Appendix*, Fig. S7).

One possible mode of binding of dimeric IF_1 that has not been considered so far in the context of the possible influence of the inhibitor protein on the topography of the cristae is that one of its two active inhibitory regions could bind to an ATP synthase complex in hydrolytic mode, leaving the second inhibitory region unbound and unable to insert itself into a catalytic site in a second copy of the enzyme. Indeed, such a state might be quite common as the inhibitor could bind to all three of the possible states of the enzyme, s1, s2 and s3, and not be restricted to cross-linking adjacent s1 and s3 states. In contrast to the crosslinking of two dimers discussed above, such a binding mode would be unlikely to have a major impact on the ultrastructure of the cristae.

Concluding remarks

Mammalian ATP synthases are highly conserved in the composition and sequences of their subunits, and therefore the nature of the association between monomers in the dimeric units will also be conserved. Likewise, the compositions and structures of the ATP synthases in yeasts and fungi resemble the mammalian enzymes in many respects (30, 31). In contrast, the structures of more distant ATP synthases, described recently (32–34), differ extensively from the mammalian enzymes. For example, their PS regions are much more complex and more rigid than those in mammals, and their cristae are likely to have very different properties to those described here. The elucidation of the molecular basis of the interactions of dimers of ATP synthases in the mitochondrial cristae of mammals, as well as those in more distant species warrant further study by tomography of mitochondrial membranes.

Materials and Methods

The purification of dimeric ATP synthase from bovine heart mitochondria, the preparation of cryo-em grids, data collection, pre-processing of micrographs, automated particle picking and initial particle selection by 2D classification have been described before (2). Particle data were sorted into sub-sets in which the catalytic state of each monomer in the pair was defined and classified into additional conformational sub-states within the sub-sets. Composite dimer models were constructed from monomeric models of bovine ATP synthase (2). For further details, see *SI Appendix*.

Data Availability. Protein models and electron density data have been deposited in the Protein Data Bank and the Electron Microscopy Data Bank under the following accession numbers: 7AJB (EMD-11428), 7AJC (EMD-11429), 7AJD (EMD-11430), 7AJE (EMD-11431), 7AJF (EMD-11432), 7AJG (EMD-11433), 7AJH (EMD-11434), 7AJI (EMD-11435), 7AJJ (EMD-11436), EMD-11449 to EMD-11454, EMD-11460 to EMD-11466, EMD-11472, EMD-11477, EMD-11479, EMD-11480, EMD-11484 to EMD-11487, EMD-11499 to EMD-11512, EMD-11527 to EMD-11546.

Acknowledgements This work was supported by Medical Research Council (MRC) UK Grants MR/M009858/1, MC_U105663150, and MC_UU_00015/8 (to J.E.W.). From 2013 to 2017, T.E.S. was in receipt of an MRC PhD Studentship. The cryo-electron microscopes at the University of Cambridge Department of Biochemistry were funded by Wellcome Trust Grants 202905/Z/16/Z and 206171/Z/17/Z (J.E.W. co-applicant/stakeholder). We thank D. Y. Chirgadze and colleagues (Department of Biochemistry, University of Cambridge) and Y. Chaban and staff of Electron Bio-Imaging Centre (eBIC), Diamond Light Source, for expert operation of microscopes and advice on data collection; and E. R. S. Kunji and M. Wikström for their helpful comments on the manuscript.

FIGURES

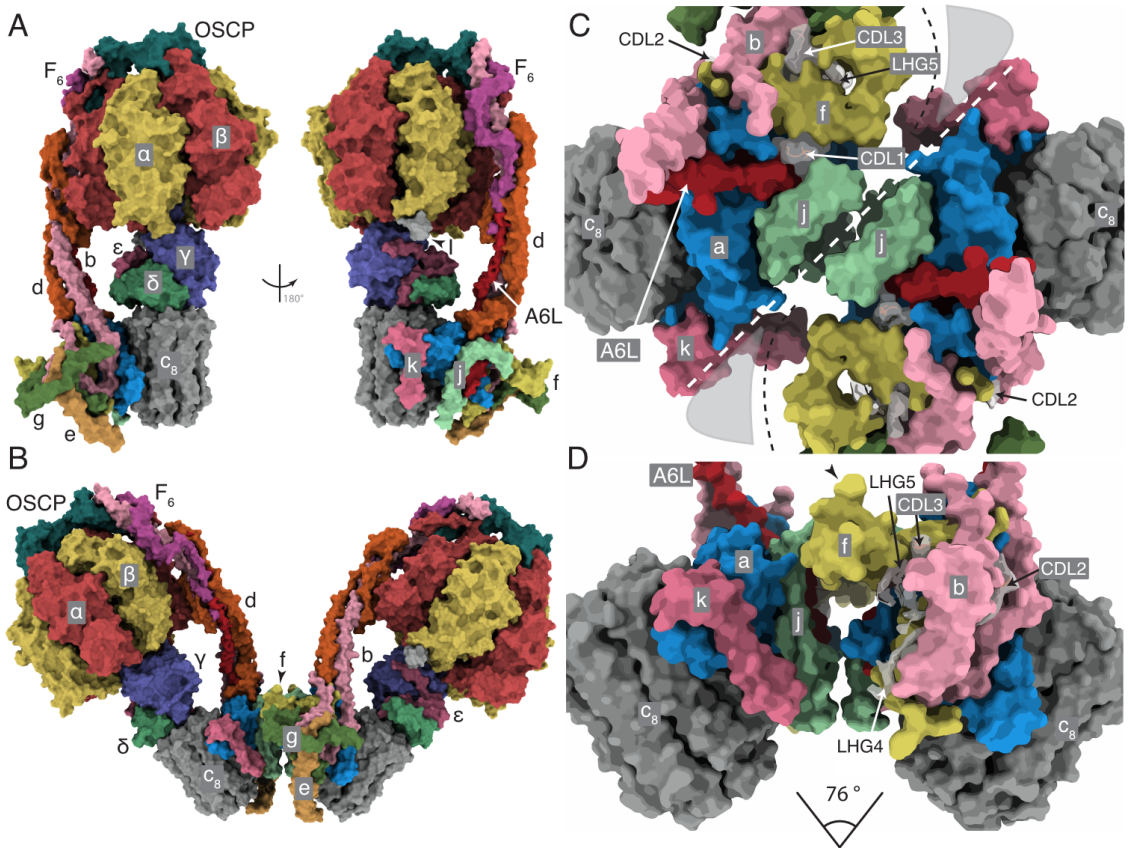

Fig. 1. The structure of the bovine ATP synthase and the monomer-monomer interfaces in the membrane domains of dimers. *A* and *B*, the structures and subunit compositions of the bovine ATP synthase monomer in rotational state 3 (PDB6ZQN (2)) and the dimer in state [s1:s1] (PDB7AJB), respectively shown as solvent excluded molecular surfaces. The s1:s1 dimer was created by docking two s1 monomers (PDB6ZPO) into the lower resolution s1:s1 dimer map. The α-, β-, γ-, δ- and ε-subunits of the F_1-catalytic domain are red, yellow, blue, indigo and green, respectively, with the central stalk (subunits γ, δ and ε) attached to the c_8-ring (dark grey) in the membrane domain in contact with subunit a or ATP6 (cornflower blue). The PS subunits, OSCP, b, d and F_6 are teal, light pink, orange and magenta, respectively, and the A6L subunit is brick red. In the region

of the monomer-monomer interface, subunits e, f, g, j and k are khaki, straw yellow, forest green, sea-foam green and dark pink, respectively. Cardiolipin (CDL) and phosphatidyl-glycerol (LHG) are transparent grey. In *A*, the monomeric complex is viewed in two rotated positions, to reveal the positions of all subunits, with the rotatory axes aligned vertically. I denotes residues 1-60 of the inhibitor protein IF_1. In *B*, the dimer is viewed from within the plane of the IMM. *C* and *D*, the solvent excluded molecular surfaces of subunits in the membrane domains of the dimeric complexes viewed between the two peripheral stalks; in *C*, the complex is viewed from the matrix side of the IMM with the monomer:monomer interfaces indicated by the white dashed line. The black dashed line denotes the protein boundary between the monomers, adjacent to a region occupied by non-specific lipids and the detergent micelle (grey shading); *D*, the orthologous view in the plane of the IMM with the monomer:monomer interfaces exposed by removal of subunits e, g and d. The angles between the axis of rotation in each monomer indicated beneath were estimated by calculating two centroids for residues 2 and 38 in each bovine c_8-ring. The axis connecting the two centroids approximates to the rotatory axis of the c-ring. The centroids and connecting axes were calculated with the Structure Measurements tool-set in Chimera (35). The angle of intersection was measured from the models aligned with these axes orthogonal to the direction of the view.

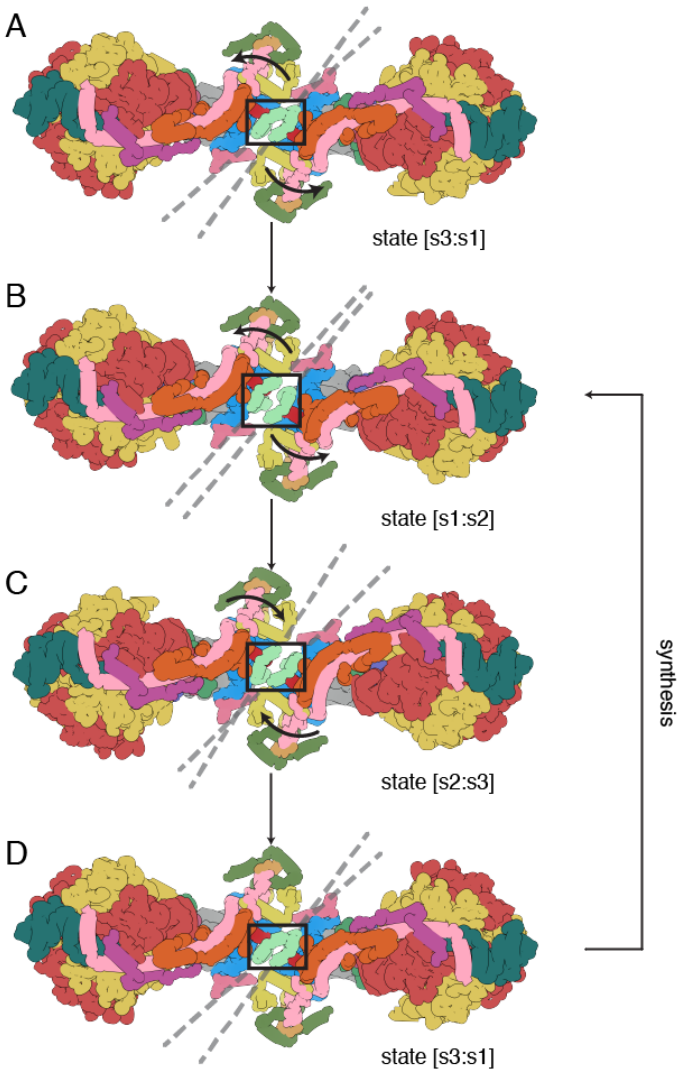

Fig. 2. Pivoting of the membrane domains of bovine ATP synthase about the matrix contact between j-subunits during ATP synthesis. Subunit j is sea-foam green inside the black box. For colors of other subunits, see the legend to Fig. 1. *A*, the state [s3:s1] dimer. Dashed lines indicate the central axis of amphipathic α-helices jH1 (residues 1-19), which lie in the plane of the matrix leaflet of the membrane. During the synthetic rotary cycle, each monomer progresses from state 1, to state 2, to state 3 and so forth. *B*, rotation of the membrane domain about the contact point in jH1 during the transition from state [s3:s1] to state [s1:s2], with accompanying displacement of subunits e, f and g, and the

transmembrane α-helices bH2 (residues 33-47) and bH3 (residues 55-73), moving the wedge outwards or inwards as indicated by the arrows. The membrane extrinsic F_1-domains remain approximately stationary, and the rocking motion associated with the asymmetry of the central stalk is transmitted to the membrane domain via the universal joint between N- and C-terminal domains of the OSCP in the PS (2); *C*, a similar pivoting motion occurs in the transition from state [s1:s2] to state [s2:s3]; *D,* completion of the rotary cycle by the transition from state [s3:s1] to state [s1:s2]. The synthetic rotary cycle continues via *B* as indicated by the arrow on the right. The scheme was constructed with composite atomic models of monomeric bovine ATP synthase, which were rigid body fitted into the consensus dimer structures produced according to *SI Appendix*, Scheme S1. This Figure relates to *SI Appendix*, Movie S3. In both this Figure and *SI Appendix*, Movie S3, side chains have been removed and secondary structure elements have been dilated to produce the diagrammatic nature of the figure, which is inferred from lower resolution structures of the intact dimeric complex.

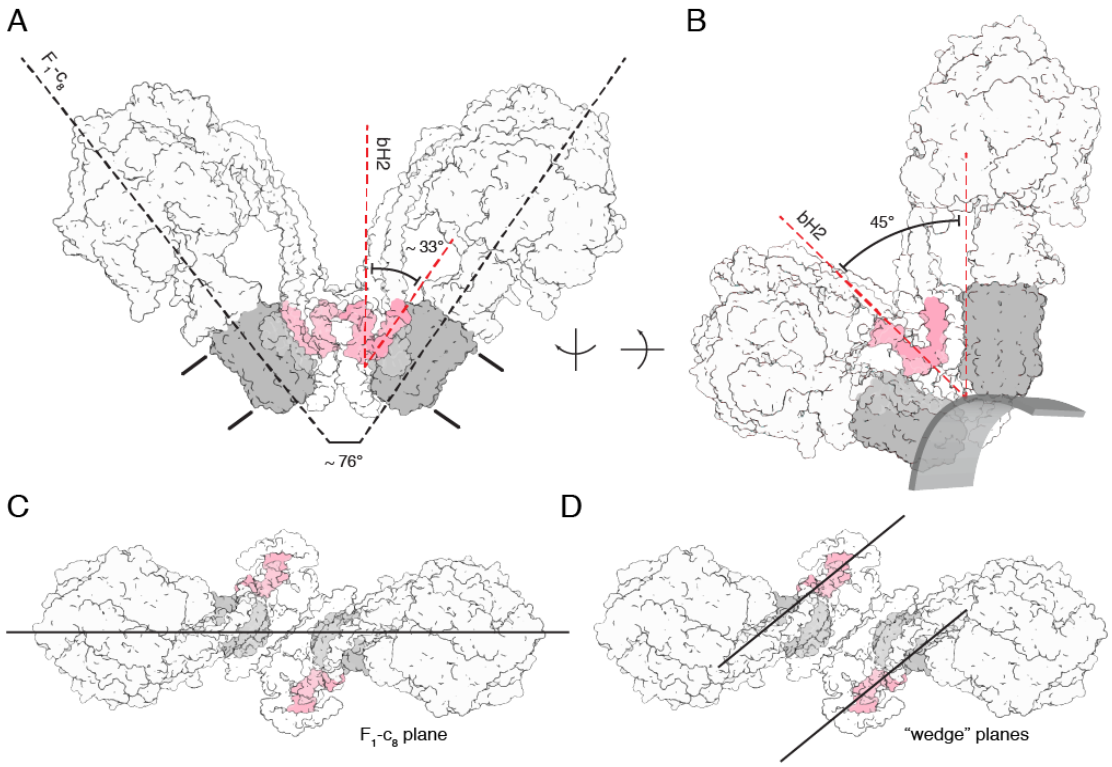

Fig. 3. Relationship between the inclined membrane wedge in the monomeric membrane domain and the association of two monomers into a dimer. The dimer in state [s2:s2] is shown. The c_8-ring is grey, and transmembrane α-helices bH2 and bH3 of subunit b (pink) define the wedge angle (2). The rest of the structure is shown in silhouette. *A,* side view showing the relationship between the angles of rotatory axes and the wedge angles when measured from the same reference point, with both rotatory axes aligned in plane. The angle between bH2 and bH3 in this view is 33°, approximately half of the dimer angle. The approximate boundary of the membrane is indicated; in *B,* the rotatory axis is aligned vertically and the structure is rotated so that bH2 and bH3 in the wedge of the right-hand monomer are in the plane of the paper. The 45° wedge angle is a measure of the inclination of the transmembrane α-helix bH2 relative to bH3 and the rotatory axis of the enzyme, as required for the wedge to provide the membrane curvature in the membrane

domain of each monomer. The approximate boundary of the lower leaflet is indicated to provide perspective; *C* and *D*, top views showing the differences between the angle measurement planes to explain why a simple doubling of the wedge angle does not produce the rotatory axis angle. In the context of the angle variations observed in the consensus reconstructions, the wedge angle and dimer, or rotatory axis, angle are separate considerations. The wedge angle does not change, rather, the way in which the membrane domains are arranged relative to one another does, as described in Fig. 2 and *SI Appendix*, Movie S3.

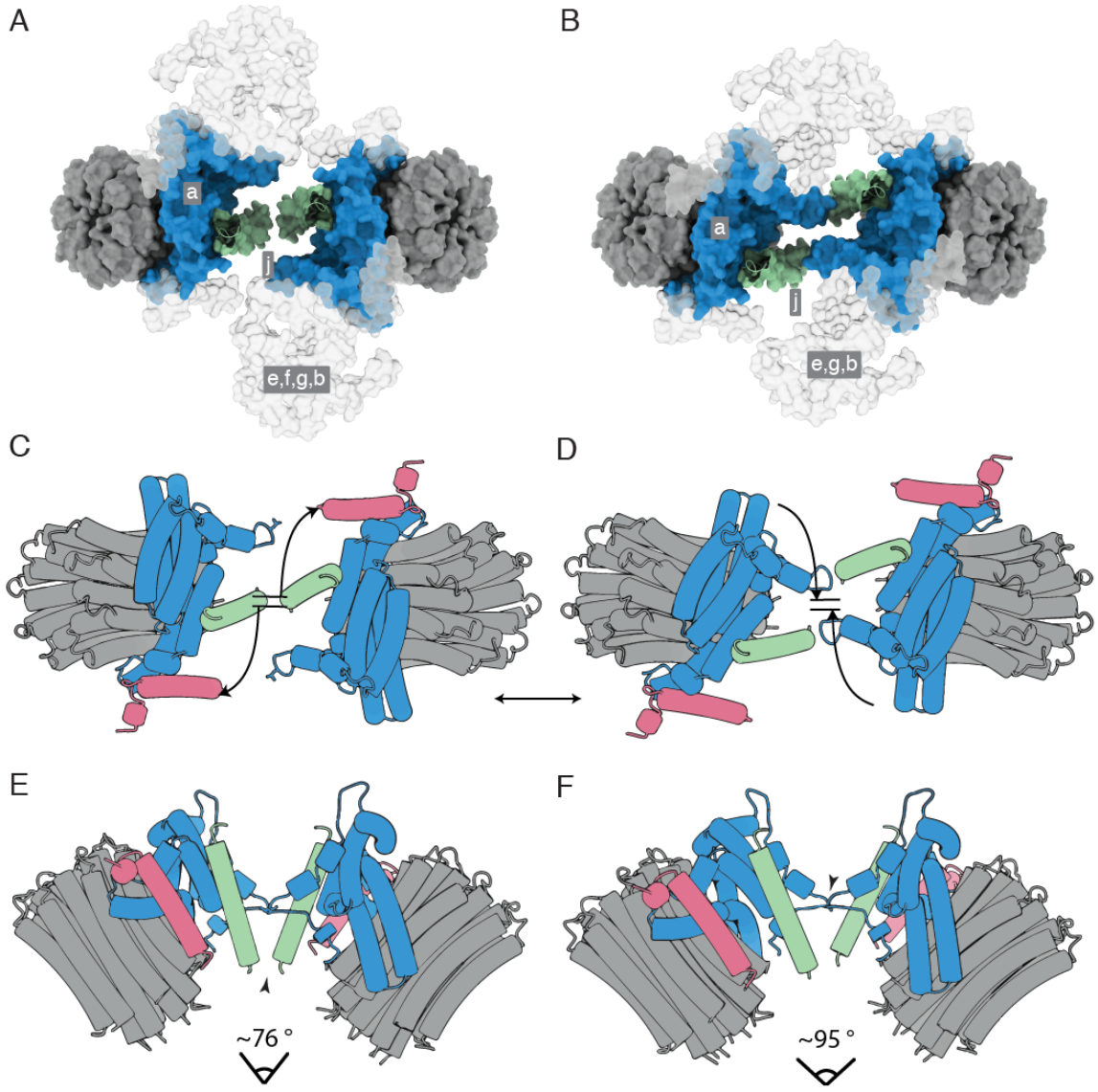

Fig. 4. Dispositions of subunits a and j in the monomer-monomer interface of dimeric bovine ATP synthase at narrowest and widest extremities of angles between rotatory axes. Subunits a, j and k are blue, green and pink, respectively, and the c_8-rings are grey. *A* and *B,* views from the matrix side of the IMM of the monomer-monomer interfaces in the membrane domains of bovine dimers with angles between rotatory axes of *ca.* 76° and *ca.* 95°, respectively. In *A* and *B*, respectively, the dimeric sub-state [s2:s2c] (see Schemes 1 and 2), and *B* in the dimeric sub-state [s2:s2b] (see Scheme 2) are shown as examples. The positions of subunits e, f, g and the membrane domain of subunit b are indicated in grey silhouette. For clarity, the F_1-domains and all PS subunits have been removed. *C*-*F*, schematic representation of the monomer-monomer interfaces, viewed in *C* and *D* as in *A* and *B*, respectively, and in *E* and *F* orthogonal to the plane of the membrane. In *E*, the arrowhead indicates an interaction between the C-terminal residues of the two j-subunits. In *F*, the arrowhead indicates a possible interaction of residues 12-19 in a loop proceeding αH1 of the a-subunit. In *C* and *D*, the curved arrows indicate the approximate compound rotation of the membrane domains that occurs as the angle of the rotatory axis changes between the dimer sub-states. This Figure relates to *SI Appendix*, Movies S5 and S6.

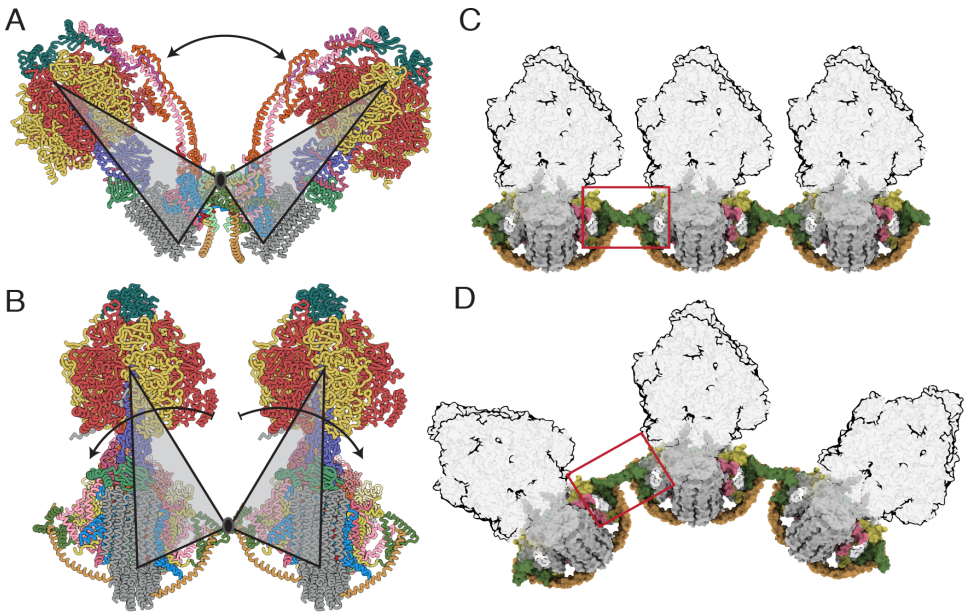

Fig. 5. Accommodation of the dimeric ATP synthase to the membrane curvature in mitochondrial cristae along the axis of oligomerization via flexible inter-dimer contacts. *A*, a view, orthogonal to the plane of the IMM, of the bovine ATP synthase dimer in state [s1:s1]. Grey triangles represent the monomers, moving back and forth as rigid bodies by rotation about their point of contact in j-subunits; the rotatory axes of both monomers are aligned in the same plane, and the arrow indicates the range of angles between rotatory axes; *B*, side view, parallel to the plane of the IMM, of two monomers in a tetrameric arrangement of two adjacent dimers formed via contacts between g-subunits. The arrows indicate the independent courses of their catalytic domains by rotation about this point; *C* and *D*, similar view to *B*, with the F_1-domains in silhouette illustrating how changes in the interface between dimers (red box) allow a curved ultra-structure to develop along the apices of the cristae. For colors of subunits, see the legend to Fig. 1.

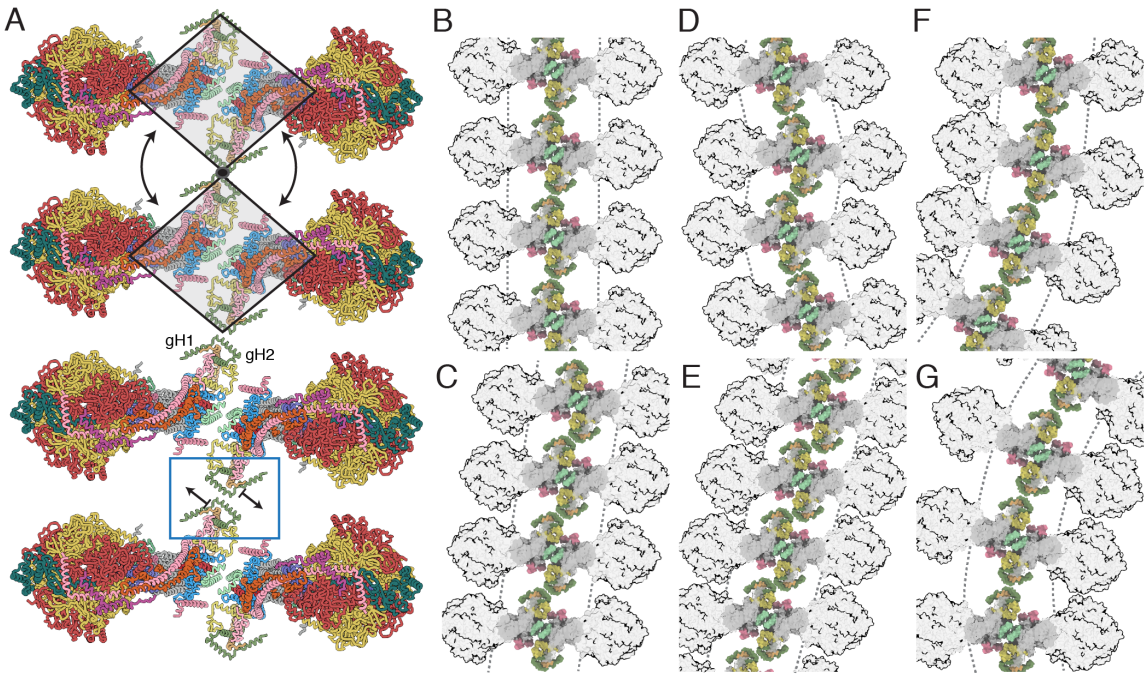

Fig. 6. Possible modes of association of dimeric bovine ATP synthases in the cristae. *A*, row of dimers viewed from above the cristae tips. In the two upper complexes, the grey trapezoids represent individual dimers moving as rigid bodies; in the lower two complexes, the individual dimers are translated as indicated by the arrows via the dimer-dimer interface in the blue box; *B*-*G*, the impact of translation or rotation of dimers on the long range order of oligomeric rows. In *B*, back-to-face stacked rows of dimers provide the simplest architecture of straight and planar oligomers. *C*, *D* and *E*, effects of dislocation of the g-g interaction at the interface between two dimers. In *C* and *E*, compact back-to-face rows of dimers to form with a range of inclinations with respect to the perpendicular axis, or, in *D*, as an alternating "zig-zag" arrangement. In *F* and *G*, bending of the rows of oligomers laterally by rotation about a fixed point at the g-g contact. More complex arrangements can be envisaged by combination of the effects in *B*-*G*, with the additional possibility of curving the membrane positively along the axis of oligomerization, as in Fig. 5*D*. For colors of subunits, see the legend to Fig. 1.

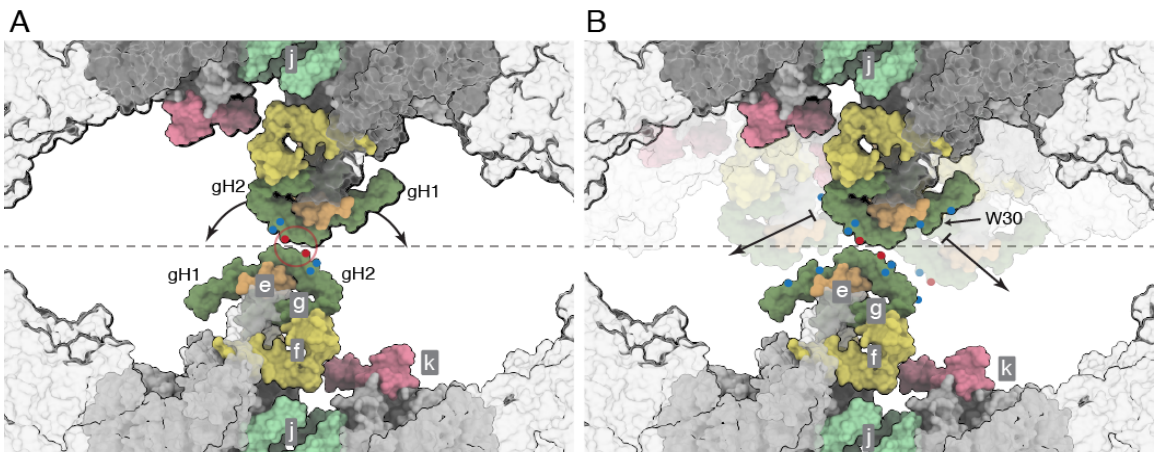

Fig. 7. Close up of the dimer-dimer interface in a possible tetrameric bovine ATP synthase. The interactions shown as a molecular surface between g-subunits in two adjacent dimers viewed from inside the mitochondrial matrix between the axes of the peripheral stalks, as in Fig. 6*B*-*G*. Portions of the catalytic domains, situated above the viewing plane, are shown in grey transparency. The grey dashed line indicates the approximate tetramer interface, which is surrounded by lipids. *A*, rotation of the dimers relative to one another, as indicated by the arrows, about a contact point between the two g-subunits, highlighted in the red circle. Key negative and positive polar residues are indicated by blue and red dots, respectively; *B*, contact dislocation of the interface between g-subunits as indicated by the arrows. Possible positions of the translocated regions are shown in transparent underlay. Residue W30 might be involved in a hydrophobic "knobs-into-holes" interaction with regions of gH1 that are rich in leucine and isoleucine residues. Additional polar residues in gH1 and gH2 are indicated by colored dots. Subunits e, f, g, j and k are khaki, straw yellow, forest green, sea-foam green and pink, respectively. The c_8-ring is grey.

References

1. J.E. Walker, ATP Synthesis by Rotary Catalysis (Nobel lecture). *Angew. Chem. Int. Ed.* **37**, 2308-2319 (1998).
2. T.E. Spikes, M.G. Montgomery, J.E. Walker, Structure of the dimeric ATP synthase from bovine mitochondria. *Proc. Natl. Acad. Sci. U. S. A.* (2020).
3. I.N. Watt, M.G. Montgomery, M.J. Runswick, A.G.W. Leslie, J.E. Walker, Bioenergetic cost of making an adenosine triphosphate molecule in animal mitochondria. *Proc. Natl. Acad. Sci. U. S. A.* **107**, 16823-16827 (2010).
4. J.E. Walker, The ATP synthase: the understood, the uncertain and the unknown. *Biochem Soc Trans* **41**, 1-16 (2013).
5. I.R. Collinson *et al.*, ATP synthase from bovine heart mitochondria. *In vitro* assembly of a stalk complex in the presence of F_1-ATPase and in its absence. *J. Mol. Biol.* **242**, 408-421 (1994).
6. I.R. Collinson, J.M. Skehel, I.M. Fearnley, M.J. Runswick, J.E. Walker, The F_1F_o-ATPase complex from bovine heart mitochondria: the molar ratio of the subunits in the stalk region linking the F_1 and F_o domains. *Biochemistry* **35**, 12640-12646 (1996).
7. A. Zhou *et al.*, Structure and conformational states of the bovine mitochondrial ATP synthase by cryo-EM. *Elife* **4**, e10180 (2015).
8. M. Sobti *et al.*, Cryo-EM reveals distinct conformations of *E. coli* ATP synthase on exposure to ATP. *Elife* **8**, (2019).
9. H. Guo, T. Suzuki, J.L. Rubinstein, Structure of a bacterial ATP synthase. *Elife* **8**, 43128 (2019).

10. M. Sobti *et al.*, Cryo-EM structures provide insight into how *E. coli* F_1F_o ATP synthase accommodates symmetry mismatch. *Nat Commun* **11**, 2615 (2020).
11. N.V. Dudkina, S. Sunderhaus, H.P. Braun, E.J. Boekema, Characterization of dimeric ATP synthase and cristae membrane ultrastructure from *Saccharomyces* and *Polytomella* mitochondria. *FEBS Lett.* **580**, 3427-3432 (2006).
12. K.M. Davies *et al.*, Macromolecular organization of ATP synthase and complex I in whole mitochondria. *Proc. Natl. Acad. Sci. U. S. A.* **108**, 14121-14126 (2011).
13. T.B. Blum, A. Hahn, T. Meier, K.M. Davies, W. Kühlbrandt, Dimers of mitochondrial ATP synthase induce membrane curvature and self-assemble into rows. *Proc. Natl. Acad. Sci. U. S. A.* (2019).
14. J. Gu *et al.*, Cryo-EM structure of the mammalian ATP synthase tetramer bound with inhibitory protein IF_1. *Science* **364**, 1068-1075 (2019).
15. G. Arselin *et al.*, The modulation in subunits e and g amounts of yeast ATP synthase modifies mitochondrial cristae morphology. *J. Biol. Chem.* **279**, 40392-40399 (2004).
16. R. Rabl *et al.*, Formation of cristae and crista junctions in mitochondria depends on antagonism between Fcj1 and Su e/g. *J. Cell Biol.* **185**, 1047-1063 (2009).
17. K.M. Davies, C. Anselmi, I. Wittig, J.D. Faraldo-Gómez, W. Kühlbrandt, Structure of the yeast F_1F_o-ATP synthase dimer and its role in shaping the mitochondrial cristae. *Proc. Natl. Acad. Sci. U. S. A.* **109**, 13602-13607 (2012).
18. J. Habersetzer *et al.*, Human F_1F_o ATP synthase, mitochondrial ultrastructure and OXPHOS impairment: a (super-)complex matter. *PLoS One* **8**, e75429 (2013).

19. C.B. Jackson *et al.*, A novel mitochondrial ATP6 frameshift mutation causing isolated complex V deficiency, ataxia and encephalomyopathy. *Eur J Med Genet* **60**, 345-351 (2017).

20. M. Oláhová *et al.*, Biallelic Mutations in ATP5F1D, which Encodes a Subunit of ATP Synthase, Cause a Metabolic Disorder. *Am. J. Hum. Genet.* **102**, 494-504 (2018).

21. S.E. Siegmund *et al.*, Three-Dimensional Analysis of Mitochondrial Crista Ultrastructure in a Patient with Leigh Syndrome by In Situ Cryoelectron Tomography. *iScience* **6**, 83-91 (2018).

22. M. Giacomello, A. Pyakurel, C. Glytsou, L. Scorrano, The cell biology of mitochondrial membrane dynamics. *Nat. Rev. Mol. Cell. Biol.* **21**, 204-224 (2020).

23. B. Daum, A. Walter, A. Horst, H.D. Osiewacz, W. Kühlbrandt, Age-dependent dissociation of ATP synthase dimers and loss of inner-membrane cristae in mitochondria. *Proc. Natl. Acad. Sci. U. S. A.* **110**, 15301-15306 (2013).

24. E. Perozo, A. Kloda, D.M. Cortes, B. Martinac, Physical principles underlying the transduction of bilayer deformation forces during mechanosensitive channel gating. *Nat. Struct. Biol.* **9**, 696-703 (2002).

25. P. Ridone *et al.*, "Force-from-lipids" gating of mechanosensitive channels modulated by PUFAs. *J Mech Behav Biomed Mater* **79**, 158-167 (2018).

26. J. He *et al.*, Assembly of the membrane domain of ATP synthase in human mitochondria. *Proc. Natl. Acad. Sci. U. S. A.* **115**, 2988-2993 (2018).

27. G. Pinke, L. Zhou, L.A. Sazanov, Cryo-EM structure of the entire mammalian F-type ATP synthase. *Nat. Struct. Mol. Biol.* **27**, 1077-1085 (2020).

28. D.M. Wolf *et al.*, Individual cristae within the same mitochondrion display different membrane potentials and are functionally independent. *EMBO J.* **38**, e101056 (2019).

29. D.W. Green, G.J. Grover, The IF_1 inhibitor protein of the mitochondrial F_1F_o-ATPase. *Biochim. Biophys. Acta* **1458**, 343-355 (2000).

30. K.R. Vinothkumar, M.G. Montgomery, S. Liu, J.E. Walker, Structure of the mitochondrial ATP synthase from *Pichia angusta* determined by electron cryo-microscopy. *Proc. Natl. Acad. Sci. U. S. A.* **113**, 12709-12714 (2016).

31. A. Hahn *et al.*, Structure of a complete ATP synthase dimer reveals the molecular basis of inner mitochondrial membrane morphology. *Mol. Cell.* **63**, 445-456 (2016).

32. B.J. Murphy *et al.*, Rotary substates of mitochondrial ATP synthase reveal the basis of flexible F_1-F_o coupling. *Science* **364**, (2019).

33. A. Mühleip, S.E. McComas, A. Amunts, Structure of a mitochondrial ATP synthase with bound native cardiolipin. *Elife* **8**, (2019).

34. R.K. Flygaard, A. Mühleip, V. Tobiasson, A. Amunts, Type III ATP synthase is a symmetry-deviated dimer that induces membrane curvature through tetramerization. *Nat Commun* **11**, 5342 (2020).

35. E.F. Pettersen *et al.*, UCSF Chimera--a visualization system for exploratory research and analysis. *J Comput Chem* **25**, 1605-1612 (2004).

PNAS
www.pnas.org

Supplementary Information for

Interface mobility between monomers in dimeric bovine ATP synthase participates in the ultrastructure of inner mitochondrial membranes

Tobias E. Spikes, Martin G. Montgomery and John E. Walker
The Medical Research Council Mitochondrial Biology Unit, University of Cambridge, Cambridge Biomedical Campus, Hills Road, Cambridge CB2 0XY, United Kingdom

Corresponding author: John E. Walker
Email: walker@mrc-mbu.cam.ac.uk

This PDF file includes:

Other supplementary materials for this manuscript include the following:

Supplementary Materials and Methods

Purification of dimeric bovine ATP synthase. The dimers were purified in the presence of glycodiosgenin, Brij-35 and phospholipids, as described elsewhere (1).

Cryo-EM data collection and processing. Grids for cryo-em containing the dimeric bovine ATP synthase were prepared and imaged by high-resolution cryo-electron microscopy as described before (1). The particle data were sorted into sub-sets in which the catalytic state of each monomer in the pair was defined (Scheme S1) and then further classified to reveal additional conformational sub-states within them (Scheme S2 and Fig. S2). The pre-processing of micrographs, automated particle picking and initial particle selection by 2D classification have been described elsewhere (1) and are summarized below in Scheme S1. Image processing procedures was performed with RELION-3.0 (2–6).

Fitting of models to density. Composite dimer models were constructed from published monomeric models of bovine ATP synthase (1), which were built and refined into focussed locally refined cryo-em reconstructions of higher resolution using COOT (7) and Phenix (8, 9) (see Table S1 and S2). They were rigid body fitted into reconstructions of the dimeric enzyme produced according to Schemes S1 and S2 using UCSF ChimeraX (10) and COOT (7). The surfaces of cryo-em reconstructions were colored according to the subunit assignments in composite dimer models as in Movies S3, S4, S5 and S6. An octomeric assembly of porcine ATP synthase (Fig. S4) was made from a re-interpreted model of porcine ATP synthase (PDB6ZNA (1), EMBD-0667 (11)).

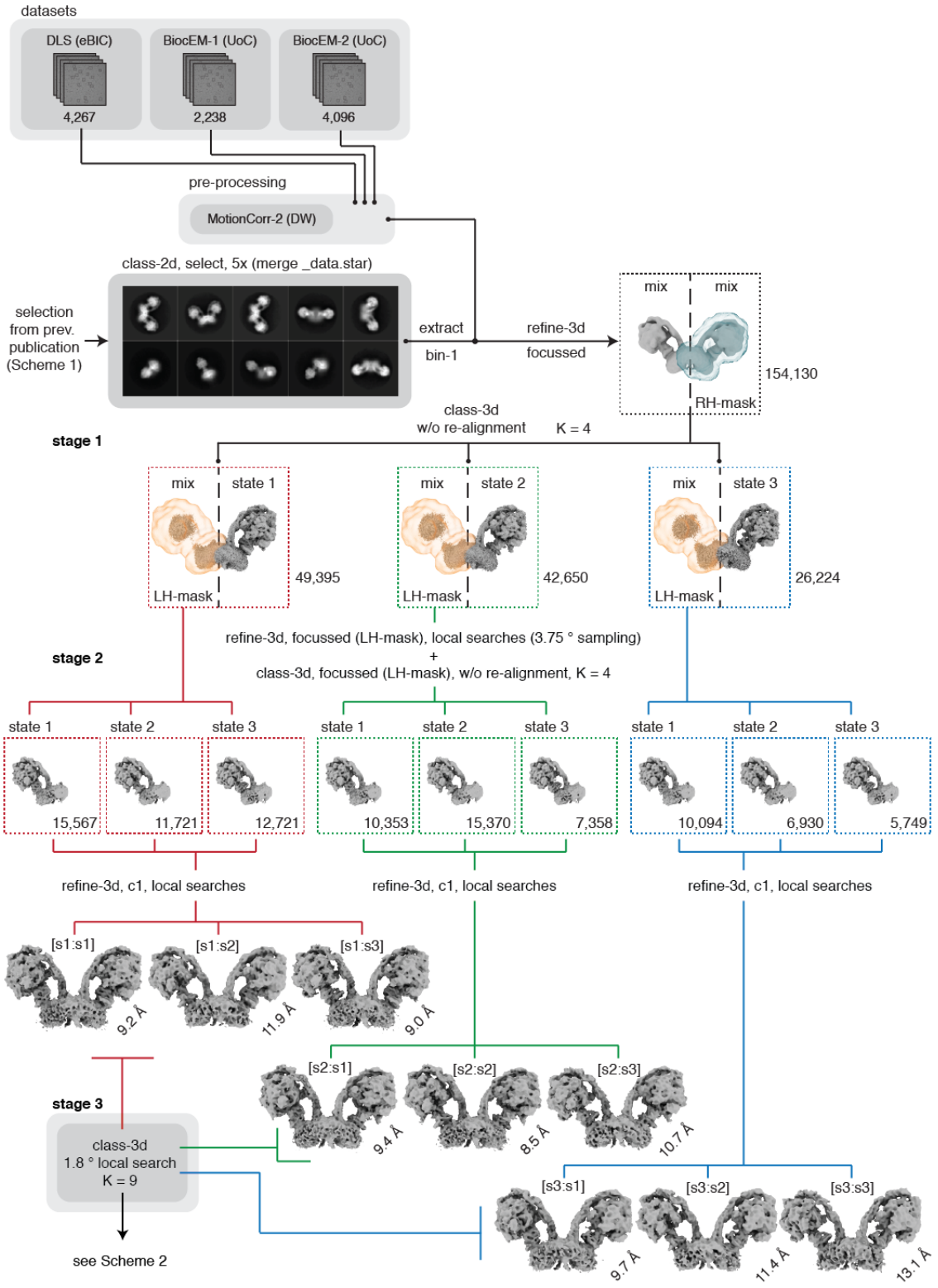

Scheme S1. Enumeration of all catalytic state combinations in dimeric bovine ATP synthase. Because the dimer particles in the data-sets were heterogeneous, high resolution structures of the intact dimer could not be determined by refinement of the whole particle set with or without the imposition of c2 symmetry. Therefore, consensus reconstructions represent an average of two distinct types of heterogeneity arising, first from the positions of the asymmetrical F_1-domain

catalytic relative to the PS in the monomeric complex, which are independent of one another, and second from variance in the spatial relationship between monomers arising from differences in the angle between the rotatory axes of the two F_1-c_8 domains. Therefore, a hierarchical classification strategy employing three stages was applied. First, the catalytic states of each half of the assembly were resolved independently, in order to provide consensus dimer reconstructions in each of the nine combinations of rotational state (shown above), Then they were resolved into classes representing distinct structural conformations with defined catalytic states (Scheme S2). Raw movie frames were corrected for motion, and were dose-weighted to improve the reconstructions in lieu of particle polishing of many individual sub-sets. 154,130 dimer particles, selected by 2D classification in a previous work (1), were re-extracted from the dose-weighted micrographs at a sampling rate of 1.048 Å/pix and separated into rotational states of the right monomer by refining the particles whilst employing a monomeric mask (blue) against the consensus dimer reference, and subsequently classifying without particle re-alignment (stage 1). This procedure yielded 49,395 particles in state-1, 42,650 particles in state-2, 26,224 particles in state 3 and 39,891 particles in a fourth class that were discarded. Each of the three classes representing the rotational states of the right molecule were refined against the consensus dimer reference with a mask encompassing the left monomer (orange). Rotation of the particles about the pseudo-twofold rotational symmetry axis was prevented by local angular searches from the orientations determined for the right monomer, thereby maintaining the relative positions of the right and left monomers with respect to the refinement reference. The left monomer was classified into the three rotational states without particle re-alignment (stage 2) from the refined orientations, leading to particle sub-sets where the rotational state of each monomer in the pair is defined, albeit with a heterogeneous relationship between their spatial arrangement in the overall assembly. The colored dashed boxes contain the number of particles in each sub-state. During this process, an additional 22,826 particles in the fourth class failed to separate into a distinct rotational state and were discarded. As before, rotation of the particles about the pseudo-c2 symmetry axis was prevented by refinement of particle sub-sets without symmetry and local searches from the previously determined orientations. These structures are shown at the bottom of the scheme and are named according to the catalytic state of the right monomer, followed by the left monomer (i.e. the order in which they were classified) as follows; states [s1:s1], [s1:s2], [s1:s3], [s2:s1], [s2:s2], [s2:s3], [s3:s1], [s3:s2] and [s3:s3] at resolutions of 9.2, 11.9, 9.0, 9.4, 8.5, 10.7, 9.7, 11.4, and 13.1 Å, respectively, with applied B-factors ranging from -215 to -500 $Å^2$. In stage 3, each particle set was classified further with reference to its respective consensus structure without particle re-alignment into nine classes (see Scheme S2).

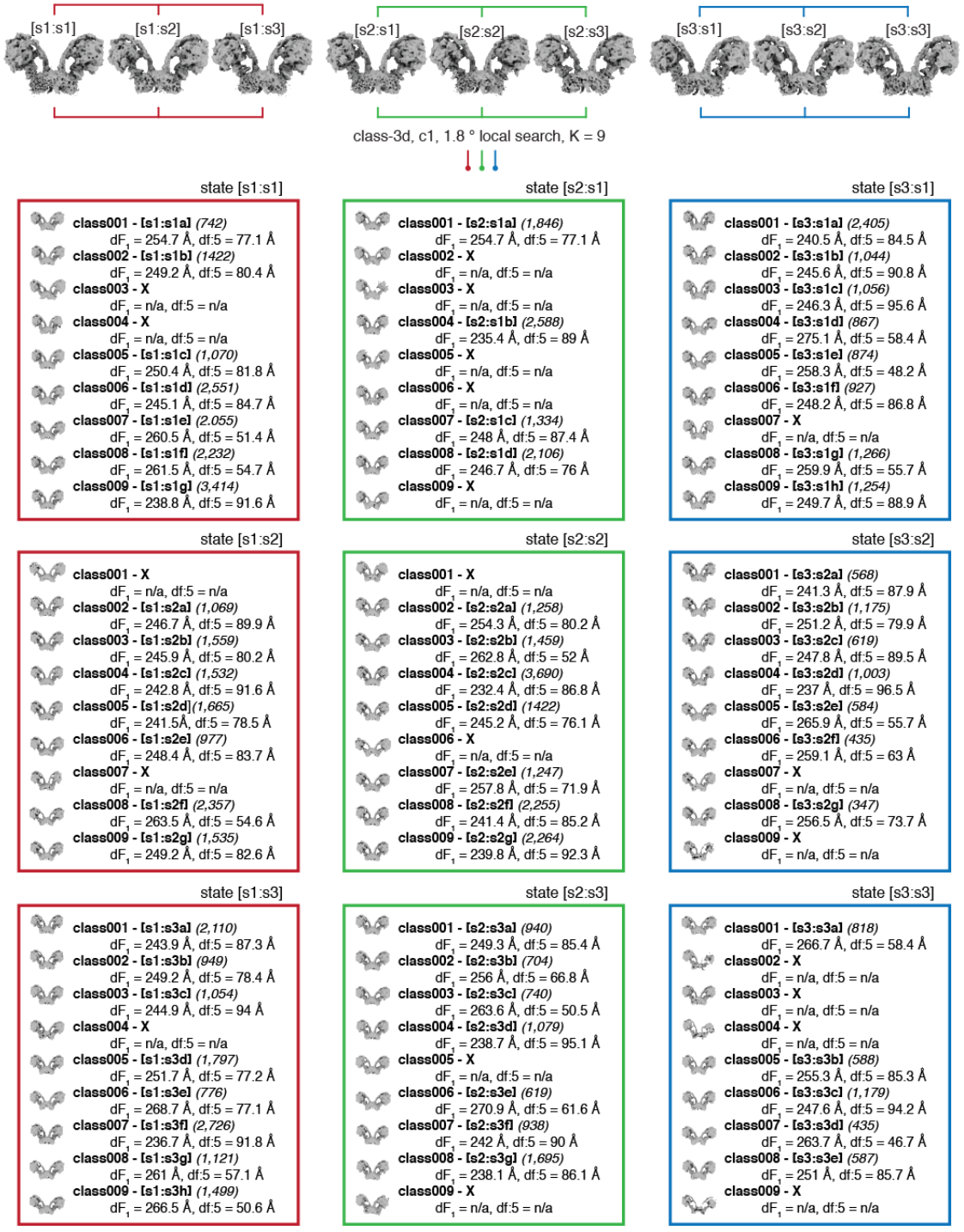

Scheme S2. Identification and analysis of structural heterogeneity in dimeric bovine ATP synthase. Each particle set represents the dimers in defined catalytic states (see Scheme S1). Local searches from the consensus orientations for alignment were enforced and the dimer particles in each set were classified into nine additional classes, shown in the colored boxes, right monomers in state 1, state 2 and state 3 in red, green and blue, respectively. The composite atomic models for the corresponding rotational state in each half of the molecule were rigid body fitted into the reconstructions. Two centroids, representing the catalytic domain and residue 5 of subunit f in a small matrix protrusion, were calculated in each monomer and the distances between them in each dimer were measured. This pair of distances, dF_1 and df:5, serve as proxy for measurements

of the angle between the rotatory axes. These measurements in Ångströms accompany the number of particles (brackets) and a map identifier (square brackets). The per-particle distributions of the measurements are summarized in Fig. S3. Twenty-two maps, with too few particles or with obvious artefacts and denoted with an "X", were excluded from this analysis, leaving fifty-nine reconstructions (see Table S2).

Analysis of sequences of subunits. Pairwise comparisons of the sequences of orthologous subunits of bovine, porcine and yeast ATP synthases subunits were made with CLUSTAL O (12) on www.uniprot.org, and their secondary structures were predicted with PSIPRED (13, 14).

Production of Figures, movies and animations. Figures and movies were prepared with USCF ChimeraX (10).

Movie S1. Structural heterogeneity in dimeric bovine ATP synthase associated with catalysis. Two copies of the atomic model of the bovine membrane domain (6ZBB) were rigid body fitted into the cryo-em density of the state [s2:s2] consensus dimer reconstruction and a simulated 7 Å density was produced from both chains of subunits a and j. Then, each of the other consensus dimer reconstructions produced by stage 2 of the hierarchical classification procedure (Scheme S1) were fitted to this simulated density so that the maps were aligned by the membrane domains, and the movie was produced by cross-fading between the different reconstructions in the following order; state [s1:s3], [s3:s1], [s1:s2], [s2:s3], [s3:s2], [s2:s1], [s1:s1], [s2:s2], [s3:s3], [s1:s1].

Movie S2. The rotary cycle during synthesis and hydrolysis. This movie was produced in the same manner as Movie S1 except that the composite atomic model of the corresponding rotational state, PDB6ZPO, PDB6ZQM and PDB6ZQN (1) for states 1, 2 and 3, respectively, in each monomer was fitted into the consensus reconstruction and the surface of each subunit was colored accordingly.

Movie S3. Pivoting of the membrane domains of adjacent monomers of bovine ATP synthase about the matrix contact between j-subunits during catalysis. This movie was produced in the same manner as Movies S1 and S2 except that the composite atomic model of the corresponding rotational state, PDB6ZPO, PDB6ZQM and PDB6ZQN (1) for states 1, 2 and 3, respectively, in each monomer was fitted into the appropriate consensus reconstruction and the surfaces of the cryo-em densities were hidden. Side chains were hidden from the atomic model, and the secondary structure elements were dilated in appearance. The movie was produced by cross-fading between the different models in the order state [s1:s2] > [s2:s3] > [s3:s1] > [s1:s2] and as described in the legend of Movie S3.

Movie S4. The fluidity, independent of catalysis, of the monomer:monomer interface at rotatory axis angles less than or equal to 90°. Composite atomic models of the bovine ATP synthase monomer in rotational state 2 (PDB6ZQM (1)) were rigid body fitted into the dimer sub-state [s2:s2c] reconstruction, in which the angle between rotatory axes is *ca.* 76°, produced by stage 3 of the hierarchical classification (see Schemes S1 and S2). A simulated 7 Å density was created from the model of the left monomer (with respect to the screen viewing direction) to which were fitted the reconstructions of the [s2:s2f] and [s2:s2g] dimer sub-states, aligning the reconstructions to a single monomer. Copies of the state 2 atomic model (PDB6ZQM (1)) were fitted into the remaining monomer domains and the surfaces of individual subunits were colored according to their position in the atomic model.

Movie S5. Trajectory, independent of catalysis, towards the formation of a wide angle between the central axes of the F_1-c_8 domains in a dimer of ATP synthase. Composite atomic models of the bovine ATP synthase monomer in rotational state 2 (PDB6ZQM (1)) were rigid body fitted into the sub-state [s2:s2c] reconstruction, in which the angle between rotatory axes is *ca.* 76°,

produced by stage 3 of the hierarchical classification (see Schemes S1 and S2). A simulated 7 Å density was created from both chains of subunit a and subunit j to which were fitted the reconstructions of the [s2:s2a], [s2:s2e] and [s2:s2b] dimer sub-states, to align them by their membrane domains. Then each reconstruction was re-sampled onto the coordinate system of the [s2:s2c] sub-state and the densities were interpolated in the order sub-state [s2:s2c] > sub-state [s2:s2a] > sub-state [s2:s2e] > sub-state [s2:s2b]. Copies of the state 2 composite atomic model (PDB6ZQM (1)) were fitted into the new positions of the sub-state reconstructions, and the positions of the atomic coordinates of each model were similarly interpolated over an equal number of frames, in the same order. In each frame of the interpolated trajectory, the surfaces of subunits were colored in the reconstructions.

Movie S6. Detailed view of the interface rearrangement, independent of catalysis, arising in the trajectory towards the wide angle dimeric ATP synthase. Top view, as viewed from the matrix, of subunit a and residues 19-49 of subunit j progressing along the interpolated atomic model trajectory from sub-state [s2:s2c] > [s2:s2a] > [s2:s2e] > [s2:s2b]. The movie was prepared as described in the Supplementary Information, Production of Movies, for Movie S5.

Movie S7. Catalytic and structural heterogeneity in purified dimeric bovine ATP synthase. All sub-states identified by the hierarchical classification strategy described in Scheme S2 are shown. They were fitted manually to one another by aligning them approximately via their membrane domains. They are cycled in alphanumerical order starting from sub-state [s1:s1a].

Supplementary Figures

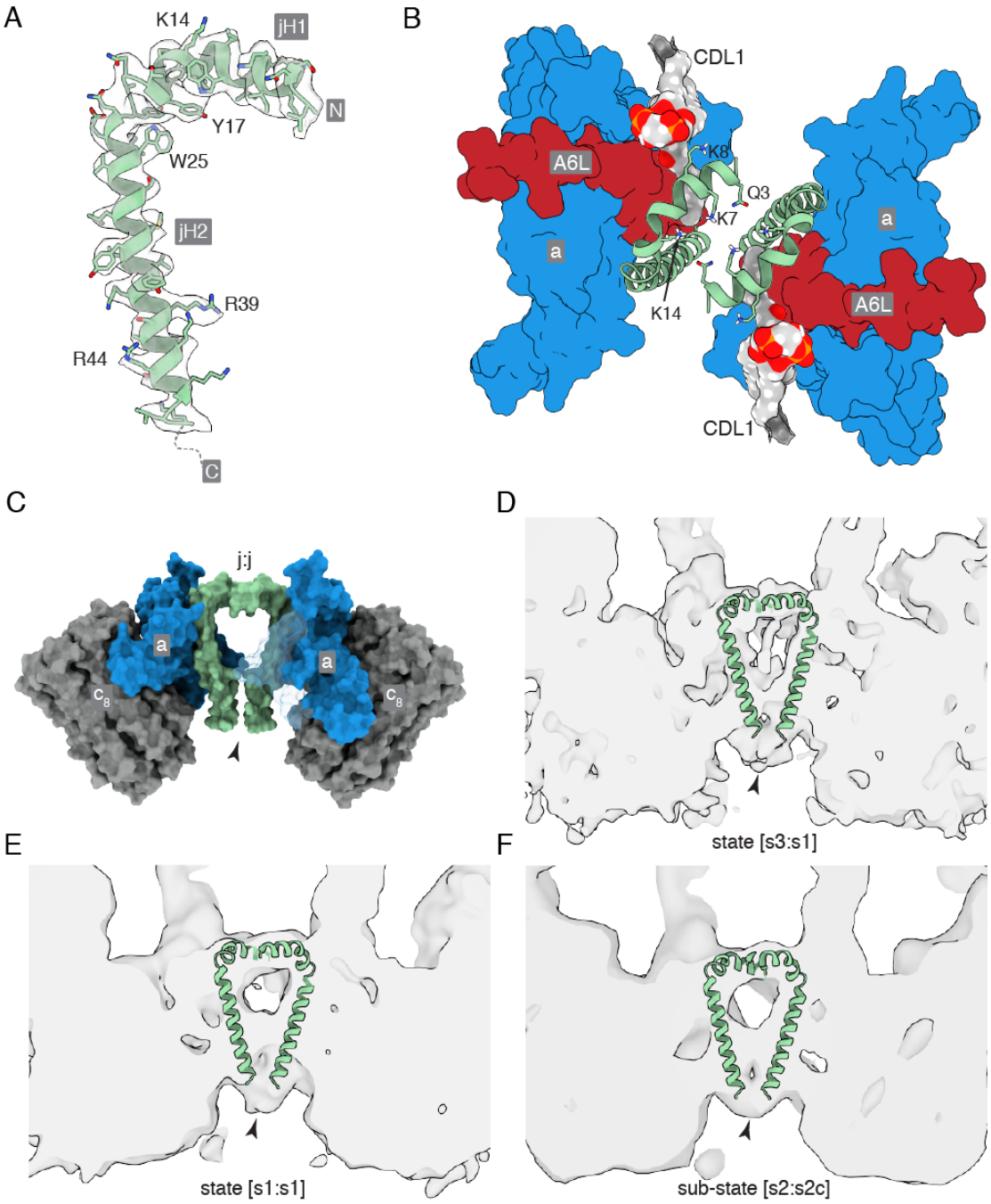

Fig. S1. The topology of subunit j in dimeric bovine ATP synthase. *A,* side view of the cryo-em density of the subunit j (grey transparency, EMD-11149) and the fitted atomic model (sea-foam green, PDB6ZBB)(1). Residues used to determine the sequence register during model building and their corresponding densities are labelled. The N-terminus of subunit j is folded into an amphipathic α-helix jH1 (residues 1-20), which lies in the lipid head group region on the matrix side of the IMM, followed by the transmembranous jH2 which lies adjacent to A6L and is associated with subunit a. The C-terminal region of jH2 (residues 40-49), protrudes into the IMS, indicated in *C* by the arrowhead; *B*, top view, from inside the mitochondrial matrix between the two peripheral stalks of the dimer (not shown), with the a-subunit (cornflower blue) and A6L-subunit (brick red) shown as a

molecular surface and the j-subunit (sea-foam green) in cartoon. The negatively charged headgroup of CDL1 (grey surface, colored by heteroatom) is bound to jK8, and to residues fQ38 and fY42 of the f-subunit in the wedge (not shown) and residues aT33, and A6LK27 and A6LK30. Residues jQ3, jK7 and jK14 are shown projecting toward the interface; *C*, side view, rotated 90° into the plane of the paper with respect to *B*, of the molecular surfaces of the a-subunit (cornflower blue) and the j-subunit (sea-foam green), and the c_8-ring (grey), in the dimeric membrane domain of the bovine ATP synthase; *D-F,* cross-sectional side views of three bovine ATP synthase dimers that exemplify density, attributed to the C-terminal regions of the j subunits, beyond the modelled residues. The state [s3:s1], state [s1:s1] and sub-state [s2:s2c] dimers are shown in *D*, *E* and *F*, respectively. The modelled regions of the j-subunits are overlayed onto the transparent density.

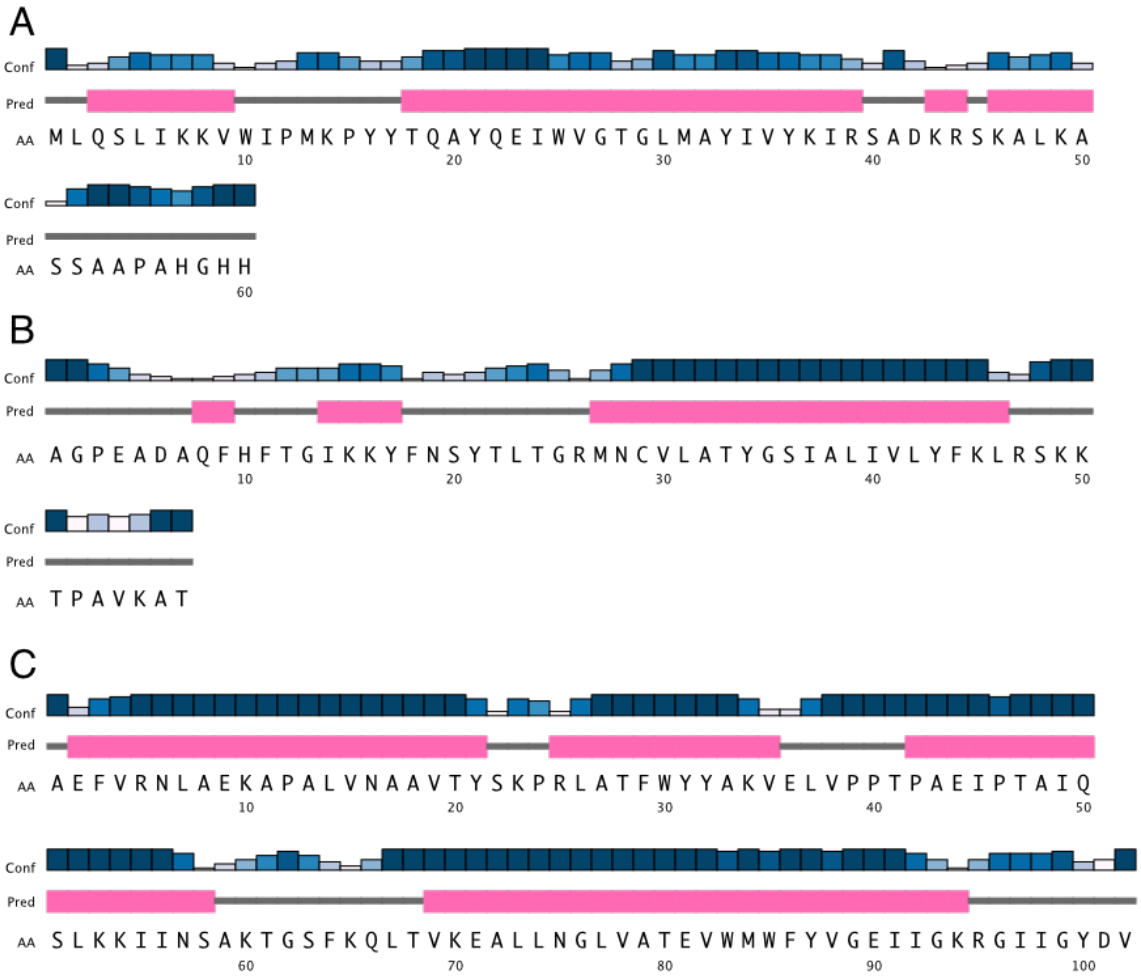

Fig. S2. The predicted secondary structures of subunits j, k and g of bovine ATP synthase. In *A*, *B* and *C*, the sequences of subunits j, k and g, respectively, are given in single letter amino acid code, and their predicted secondary structure elements and per-residue confidence scores are shown, respectively, in the lower, middle and upper rows of each panel. α-Helices are pink, and extended structures grey. Confidence scores are shown on a white-blue color scale, with dark blue being the most confident. The secondary structure predictions were performed with PSIPRED (14, 15). In the structure of bovine subunit j, residues 1-20 form an amphipathic α-helix (jH1) that lies in the plane of the IMM side leaflet and residues j22-39 form the transmembrane region of jH2. The C-terminal region of jH2 (residues 40-49) protrudes into the IMS. The rest of the sequence, comprising residues j50-60, was not modelled but is predicted to form an extended structure as shown above.

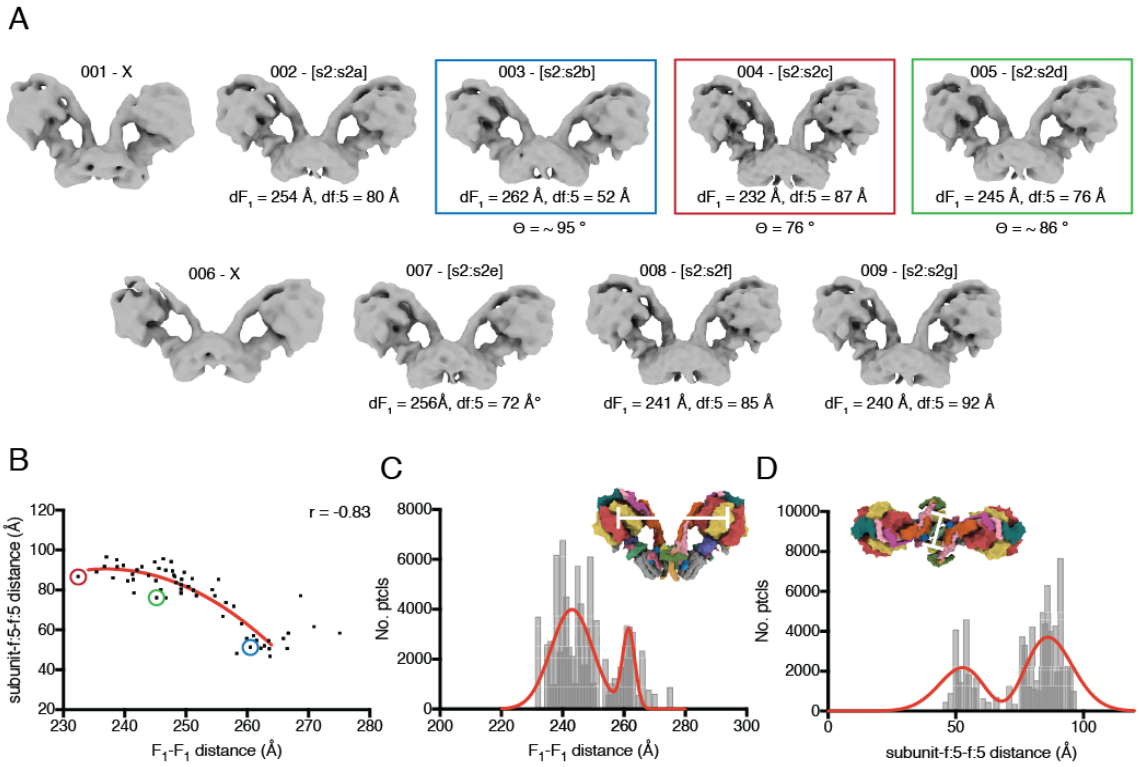

Fig. S3. Quantitation of the structural heterogeneity observed in dimeric bovine ATP synthase. *A*, stage 3 of the hierarchical classification (see Schemes 1 and 2) for dimer particles in catalytic state [s2:s2]. Particles in class 001 and 006 were discarded; Movies S3, and S4 and S5, are derived from reconstructions of sub-states [s2:s2c], [s2:s2f] and [s2:s2g], and [s2:s2c], [s2:s2a], [s2:s2e] and [s2:s2b], respectively; *B*, correlation between the distance between F_1-domains and the width of the membrane. Encircled dots correspond to the maps in colored boxes in *A*. As the angle between the rotatory axes increases, the catalytic domains separate requiring the dimer interface to re-arrange, leading to the membrane domain becoming narrower in the direction perpendicular to the plane of the rotatory axes (as in *D, Inset*). *C* and *D*, distribution of the distances between F_1-domains and between residues 5 in f-subunits, respectively. The most abundant inter-F_1 distances clustered at *ca.* 240 Å, and the distance between residues 5 in f-subunits was *ca.* 80-90 Å, which corresponds to a range of angles between rotatory axes of *ca.* 76-86°. In *C* and *D*, the insets show the approximate points of measurement.

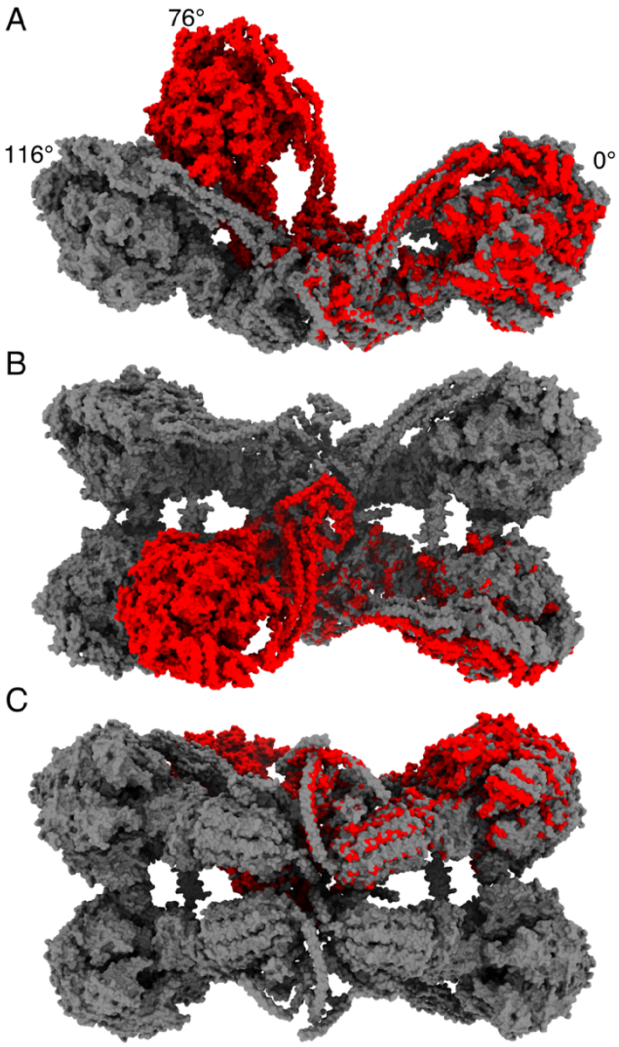

Fig. S4. Comparison of the angles between monomers in bovine dimers and porcine tetramers of ATP synthase. The porcine tetramer (grey, PDB6J5K) consists of the state [s1:s3] and [s3:s1] dimers. The model of the bovine state [s1:s3] dimer (red, PDB 7AJD) has been superimposed onto one of the s3 monomers of the porcine tetramer via their a-subunits. The models are displayed in surface representation. *A, B,* and *C,* views along the plane of the membrane, from above, and below, respectively. The membrane subunits of the porcine enzyme appear to be folding in on themselves probably because the removal of lipids during extraction of the complex with detergent causes a rearrangement of the membrane subunits thereby increasing the angle between monomers. A similar comparison cannot be made with the ovine tetramer as neither the map nor the model is publicly available.

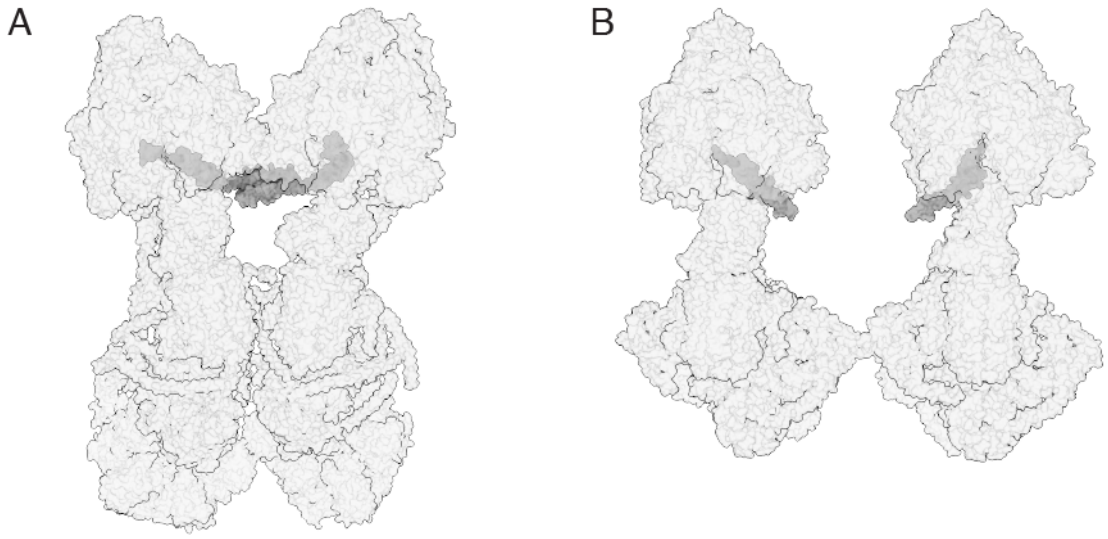

Fig. S5. Comparison of the arrangement of adjacent dimers in tetramers of porcine and bovine ATP synthase. *A,* side view of the deposited porcine tetramer model (PDB6J5K) (11) in which a pair of monomers in two adjacent dimers are oriented in the viewing plane. Inhibitor protein IF_1 is shown in solid grey and all other subunits are in grey transparency. The second pair of monomers projects away from the viewing plane. In this tetrameric arrangement, each adjacent catalytic domain is linked by a dimer of IF_1. This tethering of catalytic domains reduces the distance between the monomers and gives rise a significant tilt in the rotatory axes. It appears from the deposited structure that this tilting requires a significant rearrangement of the membrane domain in the region of the dimer-dimer interface. *B,* an equivalent view of a hypothetical bovine tetramer in the planar oligomeric arrangement suggested in Fig. 6B. This figure was generated by approximately placing models of the state [s1:s3] and [s3:s1] dimers (PDB7AJD and PDB7JH, respectively) according to the dimer-dimer interface suggested in Fig. 7A, with a small contact between adjacent regions of gH2. This distance represents the furthest point between dimers that could maintain a labile association in an oligomeric row. Note that this arrangement increases the distance significantly between each of the β_{DP}-subunits which are part of the $\alpha_{DP}\beta_{DP}$-catalytic interface that binds I1-60. See also *SI Appendix* Fig. S7.

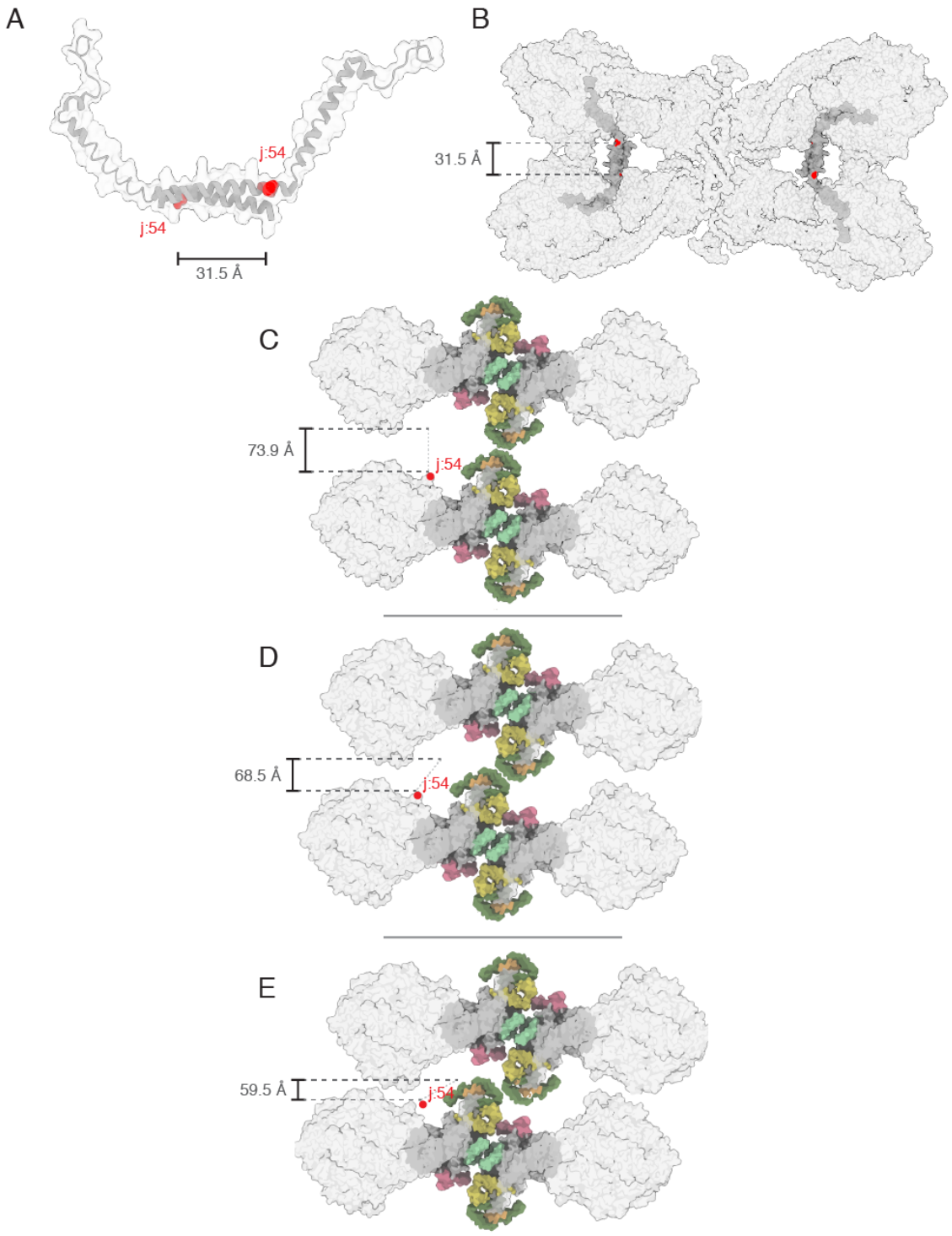

Fig. S6. Comparison of the inter-dimer distances between residues 54 of IF_1 in tetramers of porcine and bovine ATP synthase. *A,* the atomic model of dimeric porcine IF_1 (PDB6J5K) (11) shown in grey cartoon with a transparent overlay of the solvent excluded surface. Residues 54 are colored red and the distance between them is given in Ångstroms. *B,* a view from within the matrix and between the peripheral stalks of the atomic model of the porcine tetramer (PDB6J5K) showing

the *in situ* arrangement of the IF_1 dimer. IF_1 is shown in solid grey and all other subunits are shown in grey transparency. *C,* the same view of the proposed bovine tetramer in the planar oligomeric arrangement suggested by Fig. 6B. Models of the state [s1:s3] and [s3:s1] dimers (PDB7AJD and PDB7JH, respectively) were placed approximately according to the 2D arrangement in Fig. 6B, and the distance between residue 54 in each I1-60 molecule was measured in ChimeraX. The distance is indicated in Ångstroms. *D,* the tetrameric arrangement and I1-60 distance according to the oligomeric arrangement in Fig. 6C or D. *E,* the tetrameric arrangement and I1-60 distance according to the oligomeric arrangement in Fig. 6E. Note that reducing the distance between adjacent catalytic domains in this manner, that is, without rearrangement of the dimeric membrane domain, results in a translation of one dimer with respect to the other and similarly translating the position of the protruding inhibitor protein (light grey dotted line). Thus, these oligomeric arrangements are incompatible with the binding of dimeric IF_1 in absence of a significant rearrangement of the membrane domain or of the ultrastructure of the inner membrane. As detailed in Fig. S3, those dimeric structures with wider angles between their rotatory axes have correspondingly narrower membrane domain footprints, and this effect could permit closer stacking of oligomers. However, as noted in the Discussion section, it is highly unlikely that inactive tetramers and active dimers (and oligomers and so on) co-exist within a single mitochondrial crista.

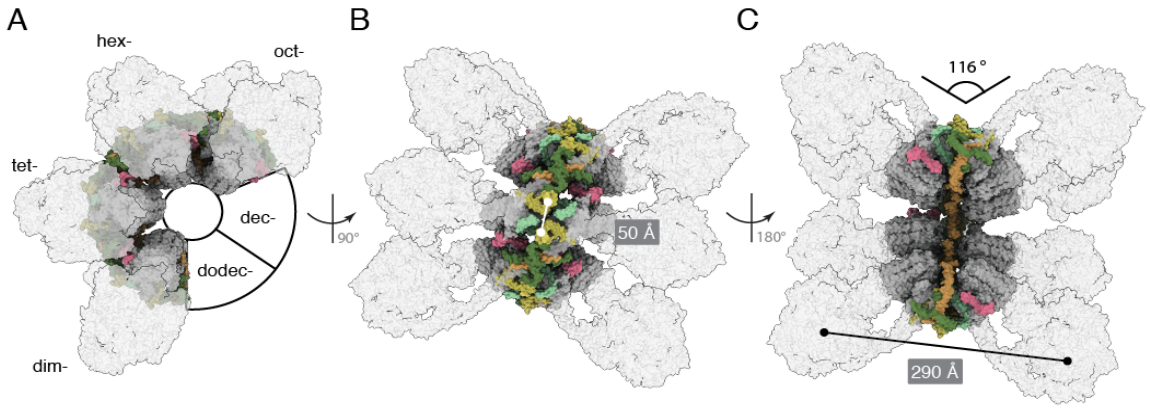

Fig. S7. Model of oligomeric porcine ATP synthase. An octomer of the reinterpreted porcine ATP synthase (PDB6ZNA) (1) was constructed by aligning two overlapping tetramers with one another and repeating the process for four dimeric units whilst maintaining the spatial relationship observed in the reported tetrameric assembly reconstruction (EMB-0667) (11). *A*, side view of the oligomer which forms a closed loop within six dimeric units if the compact tetramer interface is maintained strictly. We suggest that the formation of a tetramer and therefore of higher oligomers, in the presence of dimeric IF_1 and the absence of a native membrane environment, in this way also contributes to the large F_1-F_1 distance, narrow of the membrane domain and very wide rotatory axis observed in the structure of the porcine tetramer. These factors are closely related to the specific membrane domain organization at the interface between monomers. *B*, top view of the oligomer, with the subunit-f:5-subunit-f:5 distance labelled. *C*, a 180° rotated view of *C* with the F_1-F_1 distance labelled. These measurements can be compared with those in Scheme 2 and Fig. S2 as a proxy for the rotatory axis angle, which was measured as *ca.* 116° by the method described in Fig. 1, but was not measured for all bovine sub-states.

Table S1. Published structures employed in this work

	PBD	EMDB	Description	Reference
State 1	6YY0	EMD-11001	Bovine ATP synthase catalytic and rotor domains in rotational state 1	a
State 2	6Z1R	EMD-11039	Bovine ATP synthase catalytic and rotor domains in rotational state 2	a
State 3	6Z1U	EMD-11040	Bovine ATP synthase catalytic and rotor domains in rotational state 3	a
F_o	6ZBB	EMD-11149	Bovine ATP synthase monomeric membrane domain	a
State 1 composite	6ZPO	EMD-11342	Complete bovine ATP synthase monomer in rotational state 1	a
State 2 composite	6ZQM	EMD-11368	Complete bovine ATP synthase monomer in rotational state 2	a
State 3 composite	6ZQN	EMD-11369	Complete bovine ATP synthase monomer in rotational state 3	a
Porcine F_o	6ZMR	EMD-0668	Porcine ATP synthase monomeric membrane domain, reinterpreted	a, b
Porcine F_o tetramer	6ZNA	EMD-0667	Porcine ATP synthase tetrameric membrane domain, reinterpreted	a, b

a, Spikes *et al*, 2020; b, Gu *et al*, 2020

Table S2. Deposited data-sets relating to the structure of the dimeric bovine ATP synthase

	EMDB	PDB	Resolution (Å)	B-factor (Å^2)	Num. particles	Detail	Comment
State [s1:s1]	EMD-11428	7AJB	9.20	-300 [1]	15,567	Hierarchical classification of all dimer particles (Scheme 1)	Consensus, catalytically homogenous, structurally heterogenous
State [s1:s2]	EMD-11429	7AJC	11.9	-300 [1]	11,721	〃	〃
State [s1:s3]	EMD-11430	7AJD	9.00	-260 [1]	12,721	〃	〃
State [s2:s1]	EMD-11431	7AJE	9.40	-255 [1]	10,353	〃	〃
State [s2:s2]	EMD-11432	7AJF	8.45	-215 [1]	15,370	〃	〃
State [s2:s3]	EMD-11433	7AJG	10.7	-224 [1]	7,358	〃	〃
State [s3:s1]	EMD-11434	7AJH	9.70	-350 [1]	10,094	〃	〃
State [s3:s2]	EMD-11435	7AJI	11.4	-265 [1]	6,930	〃	〃
State [s3:s3]	EMD-11436	7AJJ	13.1	-500 [1]	5,749	〃	〃
Sub-state [s1:s1a]	EMD-11448		20.1	unsharpened [2]	742	Classification of state [s1:s1] consensus particles, K = 9, class001 (Scheme 2)	wide rotatory axis angle, subunit j not resolved
Sub-state [s1:s1b]	EMD-11449		17.5	〃	1,422	Classification of state [s1:s1] consensus particles, K = 9, class002 (Scheme 2)	intermediate rotatory axis angle, subunit j partially resolved
Sub-state [s1:s1c]	EMD-11450		18.1	〃	1,070	Classification of state [s1:s1] consensus particles, K = 9, class005 (Scheme 2)	narrow rotatory axis angle, subunit j C-terminus resolved

Sub-state [s1:s1d]	EMD-11451	14.9	〃	2,551	Classification of state [s1:s1] consensus particles, K = 9, class006 (Scheme 2)	intermediate rotatory axis angle, subunit j C-terminus resolved
Sub-state [s1:s1e]	EMD-11452	16.4	〃	2,055	Classification of state [s1:s1] consensus particles, K = 9, class007 (Scheme 2)	wide rotatory axis angle, subunit j not resolved
Sub-state [s1:s1f]	EMD-11453	15.9	〃	2,232	Classification of state [s1:s1] consensus particles, K = 9, class008 (Scheme 2)	wide rotatory axis angle, subunit j not resolved
Sub-state [s1:s1g]	EMD-11454	13.8	〃	3,414	Classification of state [s1:s1] consensus particles, K = 9, class009 (Scheme 2)	narrow rotatory axis angle, subunit j C-terminus resolved
Sub-state [s1:s2a]	EMD-11460	17.5	unsharpened	1,069	Classification of state [s1:s2] consensus particles, K = 9, class002 (Scheme 2)	narrow rotatory axis angle, subunit j C-terminus resolved
Sub-state [s1:s2b]	EMD-11461	16.9	〃	1,559	Classification of state [s1:s2] consensus particles, K = 9, class003 (Scheme 2)	intermediate rotatory axis angle, subunit j C-terminus resolved
Sub-state [s1:s2c]	EMD-11462	16.9	〃	1,532	Classification of state [s1:s2] consensus particles, K = 9, class004 (Scheme 2)	narrow rotatory axis angle, subunit j C-terminus resolved
Sub-state [s1:s2d]	EMD-11463	16.9	〃	1,665	Classification of state [s1:s2] consensus particles, K = 9, class005 (Scheme 2)	narrow rotatory axis angle, subunit j C-terminus resolved
Sub-state [s1:s2e]	EMD-11464	18.7	〃	977	Classification of state [s1:s2] consensus particles, K = 9, class006 (Scheme 2)	intermediate rotatory axis angle, subunit j C-terminus resolved, partial occupancy

Sub-state [s1:s2f]	EMD-11465	15.9	〃	2,357	Classification of state [s1:s2] consensus particles, K = 9, class008 (Scheme 2)	wide rotatory axis angle, subunit j not resolved
Sub-state [s1:s2g]	EMD-11466	16.9	〃	1,535	Classification of state [s1:s2] consensus particles, K = 9, class009 (Scheme 2)	intermediate rotatory axis angle, subunit j C-terminus resolved
Sub-state [s1:s3a]	EMD-11472	15.9	unsharpened	2,110	Classification of state [s1:s3] consensus particles, K = 9, class001 (Scheme 2)	intermediate rotatory axis angle, subunit j C-terminus resolved
Sub-state [s1:s3b]	EMD-11473	18.7	〃	949	Classification of state [s1:s3] consensus particles, K = 9, class002 (Scheme 2)	intermediate rotatory axis angle, subunit j C-terminus resolved not resolved
Sub-state [s1:s3c]	EMD-11474	18.7	〃	1,054	Classification of state [s1:s3] consensus particles, K = 9, class003 (Scheme 2)	intermediate rotatory axis angle, subunit j C-terminus resolved, partial occupancy
Sub-state [s1:s3d]	EMD-11475	15.9	〃	1,797	Classification of state [s1:s3] consensus particles, K = 9, class005 (Scheme 2)	intermediate rotatory axis angle, subunit j C-terminus resolved
Sub-state [s1:s3e]	EMD-11476	20.2	〃	776	Classification of state [s1:s3] consensus particles, K = 9, class006 (Scheme 2)	intermediate rotatory axis angle, subunit j C-terminus resolved not resolved
Sub-state [s1:s3f]	EMD-11477	15.4	〃	2,726	Classification of state [s1:s3] consensus particles, K = 9, class007 (Scheme 2)	narrow rotatory axis angle, subunit j C-terminus resolved
Sub-state [s1:s3g]	EMD-11479	18.1	〃	1,121	Classification of state [s1:s3] consensus particles, K = 9, class008 (Scheme 2)	wide rotatory axis angle, subunit j not resolved

Sub-state [s1:s3h]	EMD-11480	16.9	〃	1,499	Classification of state [s1:s3] consensus particles, K = 9, class009 (Scheme 2)	wide rotatory axis angle, subunit j not resolved
Sub-state [s2:s1a]	EMD-11484	16.4	unsharpened	1,846	Classification of state [s2:s1] consensus particles, K = 9, class001 (Scheme 2)	wide rotatory axis angle, subunit j not resolved
Sub-state [s2:s1b]	EMD-11485	15.4	〃	2,588	Classification of state [s2:s1] consensus particles, K = 9, class004 (Scheme 2)	narrow rotatory axis angle, subunit j C-terminus resolved
Sub-state [s2:s1c]	EMD-11486	17.5	〃	1,334	Classification of state [s2:s1] consensus particles, K = 9, class007 (Scheme 2)	intermediate rotatory axis angle, subunit j C-terminus resolved
Sub-state [s2:s1d]	EMD-11487	14.9	〃	2,106	Classification of state [s2:s1] consensus particles, K = 9, class008 (Scheme 2)	narrow rotatory axis angle, subunit j C-terminus resolved
Sub-state [s2:s2a]	EMD-11499	17.5	unsharpened	1,258	Classification of state [s2:s2] consensus particles, K = 9, class002 (Scheme 2)	wide rotatory axis angle, subunit j partially resolved
Sub-state [s2:s2b]	EMD-11500	17.5	〃	1,459	Classification of state [s2:s2] consensus particles, K = 9, class003 (Scheme 2)	wide rotatory axis angle, subunit j not resolved
Sub-state [s2:s2c]	EMD-11501	12.8	〃	3,690	Classification of state [s2:s2] consensus particles, K = 9, class004 (Scheme 2)	narrow rotatory axis angle, subunit j C-terminus resolved, most homogenous
Sub-state [s2:s2d]	EMD-11502	16.4	〃	1,422	Classification of state [s2:s2] consensus particles, K = 9, class005 (Scheme 2)	intermediate rotatory axis angle, subunit j C-terminus resolved, partial occupancy

Sub-state [s2:s2e]	EMD-11503	18.1	〃	1,247	Classification of state [s2:s2] consensus particles, K = 9, class007 (Scheme 2)	wide rotatory axis angle, subunit j not resolved
Sub-state [s2:s2f]	EMD-11504	14.9	〃	2,255	Classification of state [s2:s2] consensus particles, K = 9, class008 (Scheme 2)	intermediate rotatory axis angle, subunit j C-terminus resolved
Sub-state [s2:s2g]	EMD-11505	14.9	〃	2,264	Classification of state [s2:s2] consensus particles, K = 9, class009 (Scheme 2)	intermediate rotatory axis angle, subunit j C-terminus resolved
Sub-state [s2:s3a]	EMD-11506	18.1	unsharpened	940	Classification of state [s2:s3] consensus particles, K = 9, class001 (Scheme 2)	intermediate rotatory axis angle, subunit j C-terminus resolved
Sub-state [s2:s3b]	EMD-11507	19.4	〃	704	Classification of state [s2:s3] consensus particles, K = 9, class002 (Scheme 2)	intermediate rotatory axis angle, subunit j C-terminus not resolved
Sub-state [s2:s3c]	EMD-11508	20.2	〃	740	Classification of state [s2:s3] consensus particles, K = 9, class003 (Scheme 2)	wide rotatory axis angle, subunit j not resolved
Sub-state [s2:s3d]	EMD-11509	18.1	〃	1,079	Classification of state [s2:s3] consensus particles, K = 9, class004 (Scheme 2)	narrow rotatory axis angle, subunit j C-terminus resolved
Sub-state [s2:s3e]	EMD-11510	20.9	〃	619	Classification of state [s2:s3] consensus particles, K = 9, class006 (Scheme 2)	wide rotatory axis angle, subunit j not resolved
Sub-state [s2:s3f]	EMD-11511	18.7	〃	938	Classification of state [s2:s3] consensus particles, K = 9, class007 (Scheme 2)	narrow rotatory axis angle, subunit j C-terminus partially resolved

Sub-state [s2:s3g]	EMD-11512	16.4	〃	1,695	Classification of state [s2:s3] consensus particles, K = 9, class008 (Scheme 2)	narrow rotatory axis angle, subunit j C-terminus resolved
Sub-state [s3:s1a]	EMD-11527	15.4	unsharpened	2,405	Classification of state [s3:s1] consensus particles, K = 9, class001 (Scheme 2)	narrow rotatory axis angle, subunit j C-terminus resolved
Sub-state [s3:s1b]	EMD-11528	18.1	〃	1,044	Classification of state [s3:s1] consensus particles, K = 9, class002 (Scheme 2)	intermediate rotatory axis angle, subunit j C-terminus resolved
Sub-state [s3:s1c]	EMD-11529	18.1	〃	1,056	Classification of state [s3:s1] consensus particles, K = 9, class003 (Scheme 2)	intermediate rotatory axis angle, subunit j C-terminus partially resolved
Sub-state [s3:s1d]	EMD-11530	18.7	〃	867	Classification of state [s3:s1] consensus particles, K = 9, class004 (Scheme 2)	wide rotatory axis angle, subunit j not resolved
Sub-state [s3:s1e]	EMD-11531	19.4	〃	874	Classification of state [s3:s1] consensus particles, K = 9, class005 (Scheme 2)	wide rotatory axis angle, subunit j not resolved
Sub-state [s3:s1f]	EMD-11532	18.7	〃	927	Classification of state [s3:s1] consensus particles, K = 9, class006 (Scheme 2)	intermediate rotatory axis angle, subunit j C-terminus partially resolved
Sub-state [s3:s1g]	EMD-11533	17.5	〃	1,266	Classification of state [s3:s1] consensus particles, K = 9, class008 (Scheme 2)	wide rotatory axis angle, subunit j not resolved
Sub-state [s3:s1h]	EMD-11534	17.5	〃	1,254	Classification of state [s3:s1] consensus particles, K = 9, class009 (Scheme 2)	narrow rotatory axis angle, subunit j C-terminus partially resolved

Sub-state [s3:s2a]	EMD-11535	16.9	unsharpened	568	Classification of state [s3:s2] consensus particles, K = 9, class001 (Scheme 2)	narrow rotatory axis angle, subunit j C-terminus resolved
Sub-state [s3:s2b]	EMD-11536	20.2	〃	1,175	Classification of state [s3:s2] consensus particles, K = 9, class002 (Scheme 2)	intermediate rotatory axis angle, subunit j C-terminus partially resolved
Sub-state [s3:s2c]	EMD-11537	18.1	〃	619	Classification of state [s3:s2] consensus particles, K = 9, class003 (Scheme 2)	intermediate rotatory axis angle, subunit j C-terminus resolved
Sub-state [s3:s2d]	EMD-11538	20.9	〃	1,003	Classification of state [s3:s2] consensus particles, K = 9, class004 (Scheme 2)	narrow rotatory axis angle, subunit j C-terminus partially resolved
Sub-state [s3:s2e]	EMD-11539	18.7	〃	584	Classification of state [s3:s2] consensus particles, K = 9, class005 (Scheme 2)	wide rotatory axis angle, subunit j not resolved
Sub-state [s3:s2f]	EMD-11540	20.9	〃	435	Classification of state [s3:s2] consensus particles, K = 9, class006 (Scheme 2)	wide rotatory axis angle, subunit j not resolved
Sub-state [s3:s2g]	EMD-11541	20.9	〃	347	Classification of state [s3:s2] consensus particles, K = 9, class008 (Scheme 2)	intermediate rotatory axis angle, subunit j C-terminus partially resolved
Sub-state [s3:s3a]	EMD-11542	19.4	unsharpened	818	Classification of state [s3:s3] consensus particles, K = 9, class001 (Scheme 2)	wide rotatory axis angle, subunit j not resolved
Sub-state [s3:s3b]	EMD-11543	20.9	〃	588	Classification of state [s3:s3] consensus particles, K = 9, class005 (Scheme 2)	intermediate rotatory axis angle, subunit j C-terminus not resolved

Sub-state [s3:s3c]	EMD-11544	17.5	〃	1,179	Classification of state [s3:s3] consensus particles, K = 9, class006 (Scheme 2)	narrow rotatory axis angle, subunit j C-terminus resolved
Sub-state [s3:s3d]	EMD-11545	23.8	〃	435	Classification of state [s3:s3] consensus particles, K = 9, class007 (Scheme 2)	wide rotatory axis angle, subunit j not resolved
Sub-state [s3:s3e]	EMD-11546	21.8	〃	587	Classification of state [s3:s3] consensus particles, K = 9, class008 (Scheme 2)	intermediate rotatory axis angle, subunit j C-terminus not resolved

[1] The maps were sharpened with an *ad hoc* user defined B-factor in lieu of calculating a value from the half-map data.

[2] Without map sharpening.

Table S3. Summary of the structural models of bovine subunits g, j, and k

Subunit	No. of Residues	Residues modelled
g	102	20-98
j	60	2-49
k	57	12-47

Movie legends

Movie S1 (separate file). Structural heterogeneity in dimeric bovine ATP synthase associated with catalysis. The 13 sec movie demonstrates the rocking motion of the catalytic domains as they step through the three main catalytic states and the corresponding contortions of the PS as it responds to the torque of rotation, and also the subtle changes in the spatial relationship of each monomer to the other as the enzyme cycles through catalytic states and how this changes the angle of the rotatory axis. In Movie S2, these subtle changes can be seen also by tracking the movement of subunit e (khaki) and subunit g (forest green). The range of observed angles between rotatory axes in the consensus reconstructions was *ca.* 76º to 86º. In the membrane, it is likely that these movements will be damped by the lateral pressure of the bilayer and by interactions with adjacent dimers. This damping would result in larger apparent motions of the PS and catalytic domain (which can be demonstrated by aligning monomers of state 1, state 2 and state 3 via their a-subunits, that is, by fixing the relative motion of the membrane domains). Conversely, this fluidity in the membrane domain may provide a mechanism to dampen motions caused by asymmetric rotation by reducing the net displacement of the catalytic domain.

Movie S2 (separate file). The rotary cycle during synthesis and hydrolysis. In the synthetic direction, reconstructions appear in the order state [s3:s1] > [s1:s2] > [s2:s3], and the rotor turns anticlockwise as viewed from the mitochondrial matrix; during hydrolysis with clockwise rotation, the order is reversed. This 21 sec movie complements Movie S1 by identifying the subunits of the enzyme and by displaying the reconstructions in the physiological order of catalysis. From 00:00-00:06 sec, the reconstructions are shown slowly in order, from 00:06 sec to 00:10 sec, the enzyme is undergoing synthesis, and from 00:10 sec to 00:14 sec hydrolysis. Then the sequence from 00:06 sec to 00:14 sec is repeated. Although the enzyme is inhibited by IF_1, it is possible to construct the rotary mechanism because all three states of the catalytic β-subunits, β_E, β_{DP} and β_{TP}, are present in the structure. In the intact monomer, the three-fold rotational symmetry of the mechanism is broken by the association of the PS, and the three IF_1 inhibited rotational states represent the full catalytic cycle in any of the three catalytic sites. As the maps or models appear in sequence, each catalytic site cycles through the β_E, β_{DP} and β_{TP} states during synthesis, and the reverse sense during hydrolysis. As shown in the movie, the dimeric enzyme contorts significantly during the independent rotary cycles of each monomer. The α, β, γ, δ, ε, OSCP and F_6 subunits of the membrane extrinsic domain are dull red, golden yellow, purple-blue, green, dark purple, teal and magenta, respectively. The inhibitor protein, IF_1, (grey) protrudes from the α_{DP}-β_{DP} interface in various positions. The membrane domain subunits a, A6L, b, e, f, g, j and k are cornflower blue, brick red, light pink, khaki, straw yellow, forest green, sea-foam green and dark pink, respectively. The phosphates of the lipid headgroups are bright red. The c_8-ring and remaining unmodelled density of the micelle are dark grey and light grey, respectively.

Movie S3 (separate file). Pivoting of the membrane domains of adjacent monomers of bovine ATP synthase about the matrix contact between j-subunits during catalysis. The 53 sec movie, starts with the consensus reconstruction of the ATP synthase dimer in state [s1:s2] (grey) followed by a schematic representation of the monomeric models rigid body fitted into the density. Then from 00:05 sec to 00:013 sec, the state [s2:s3] and state [s3:s1] dimers and their atomic models appear in catalytic order during synthesis. From 00:14 sec to 00:30 sec, side and top views of the enzyme highlight the rearrangement of the membrane domains during synthesis. In

particular, there is significant movement in the relative positions of subunits f (straw yellow) and g (forest green), which rotate with the rest of the membrane domain during the pivoting motion. Finally, transitions between pairs of catalytic states are alternated to accentuate each component of the total movement. From 00:30 sec to 00:37 sec are shown the transition from state [s3:s1] to state [s1:s2]; followed by the transition from state [s1:s2] to state [s2:s3] from 00:38 sec to 00:45 sec, and the transition from state [s2:s3] to state [s3:s1] from 00:45 sec to 00:53 sec; in the top view, the changes at the interface between the two j-subunits can be seen, about which the monomers pivot during the catalytic cycle. For colors of subunits and other details, see the legend to Fig. 1.

Movie S4 (separate file). The fluidity, independent of catalysis, of the monomer:monomer interface at rotatory axis angles less than or equal to 90°. The 56 sec movie depicts a transition of the state [s2:s2] sub-states from sub-state [s2:s2c] > [s2:s2f] > [s2:s2g] > [s2:s2c]. The sub-states were derived by classification of ATP synthase dimer particles in rotational state [s2:s2]. Thus, the pivoting is independent of both the action of catalysis and the associated motions described in Movies 1 and 2, although the movement mode is similar. The transitions between these sub-states demonstrate the pivoting motion about the subunit j:subunit j interface in the centre of the membrane domain, with the accompanying rearrangement of subunits e, f, g and k. In the first part of the movie (00:00 sec to 00.21 sec) a side view, in the plane of the membrane, is presented, and in the second part, from 00:22 sec to 00:40 sec, the same sub-state transitions are viewed from the mitochondrial matrix. From 00:40 sec to 00:56 sec, the view is from the IMS showing the C-terminal contact point of subunit j protruding into the IMS. Several sub-states displaying this feature were found in all consensus dimer particle sub-sets and, when combined, they represent the most abundant structural conformers in the dataset with 67.6 % of particles belonging to classes in which the reconstruction displays evidence of contact between the C-terminal regions of j-subunits. In general, the foot-print of the membrane domain of these sub-states is wider, and the angle between the central axes of the F_1-c_8 domains is narrower with a correspondingly shorter distance between F_1 domains. The membrane domain subunits a, A6L, b, e, f, g, j and k are cornflower blue, brick red, light pink, khaki, straw yellow, forest green, sea-foam green and dark pink, respectively. The c_8-ring and remaining unmodelled density of the micelle are dark grey and light grey, respectively.

Movie S5 (separate file). Trajectory, independent of catalysis, towards the formation of a wide angle between the central axes of the F_1-c_8 domains in a dimer of ATP synthase. The widening arises from a sliding and twisting of the membrane domains along the monomer-monomer interface surface provided by subunits a and j and occurs independently from the action of catalysis. The 36 sec movie displays transitions between several sub-states with more obtuse rotatory axis angles than those in the consensus reconstructions (shown in Movies S1, S2 and S3) and in the other sub-states of the state [s2:s2] dimer (see Movie S4). From 00:00 sec to 00:06 sec, the density of the dimer reconstructions is colored to match the subunit colors of the composite atomic models fitted within them (see Fig. 1). From 00:07 sec to 00:15 sec, the densities are interpolated in the following order; sub-states [s2:s2c], [s2:s2a], [s2:s2e], [s2:s2b], [s2:s 2e], then [s2:s2c] and so forth. This sequence is repeated in a view from the matrix and IMS sides of the complex from 00:19 sec 00:24 sec and 00:31 sec to 00:36 sec, respectively. The dramatic changes in the angle of the rotatory axes and the substantial rearrangement of the dimer interface thins the foot-print of the membrane domain significantly (as viewed from above or below the complex). This thinning affects how dimers of dimers and higher oligomers might form, as in this configuration subunit k is positioned closer to subunit g in an adjacent dimer. Also, the IMS protrusion of subunit j is absent, possibly because either a contact between the C-terminal regions of the subunit has been broken, or because of the lower resolution of these reconstructions. Other possible explanations are that this wide angle conformation results from the loss of one or all of the following: subunit j, CDL1, or unresolved lipids in the wedge. It is also possible that the extended structure of the C-terminal region of subunit j remains in contact, but was not resolved. This is possible, if not probable, as the distance between the last modelled residues in the subunit j protomers is *ca.* 29-38 Å at its furthest in sub-state [s2:s2b] and the C-terminal 11 residues of subunit j were not built. If the unresolved

region comprises an extended and/or a partially α-helical structure, 22 residues would be sufficient to span the distance between their C-termini.

Movie S6 (separate file). Detailed view of the interface rearrangement, independent of catalysis, arising in the trajectory towards the wide angle dimeric ATP synthase. A top view of the trajectory in Movie S5 is shown. Subunits a and j are cornflower blue and sea-foam green, respectively, and are shown as a solvent excluded surface. The 41 sec movie shows the sliding and twisting of each monomer along the monomer-monomer interface that leads to the widest of the rotatory axis angles, and the narrowest membrane domain footprint. The final part of the movie (from 31 sec) depicts the same sequence of events in a side view of the dimeric complex, shown as a solvent excluded molecular surface. This final part demonstrates how the changes in the dimer interface depicted in the first portion of the movie relate to changes of the rotatory axis between the monomers.

Movie S7 (separate file). Catalytic and structural heterogeneity in purified dimeric bovine ATP synthase. This 38 sec movie shows all the motions observed between monomers accompanying changes in rotational state, and flexions of monomers in fixed rotational states, and combinations of both. The same sequence of reconstructions appear three times at increasing speeds to demonstrate the highly dynamic nature of the assembly. From 00:00 sec to 00:18 sec, in a side view of the dimer, the reconstructions are changed at a rate of *ca.* 3 sec^{-1}. In the second part from 00:18 sec to 00:26 sec the rate is *ca.* 9 sec^{-1}. In the final segment from 27 sec to 38 sec, the rate is *ca.* 24 sec^{-1} and the complexes are viewed from the matrix. All combinations of rotational state and the extents of the relative motions of the monomers are represented.

SI References

1. T.E. Spikes, M.G. Montgomery, J.E. Walker, Structure of the dimeric ATP synthase from bovine mitochondria. *Proc. Natl. Acad. Sci. U. S. A.* (2020).
2. S.H. Scheres, RELION: implementation of a Bayesian approach to cryo-EM structure determination. *J. Struct. Biol.* **180**, 519-530 (2012).
3. S.H. Scheres, A Bayesian view on cryo-EM structure determination. *J. Mol. Biol.* **415**, 406-418 (2012).
4. R. Fernandez-Leiro, S.H.W. Scheres, A pipeline approach to single-particle processing in RELION. *Acta Crystallogr D Struct Biol* **73**, 496-502 (2017).
5. J. Zivanov *et al.*, New tools for automated high-resolution cryo-EM structure determination in RELION-3. *Elife* **7**, (2018).
6. J. Zivanov, T. Nakane, S.H.W. Scheres, Estimation of high-order aberrations and anisotropic magnification from cryo-EM data sets in RELION-3.1. *IUCrJ* **7**, 253-267 (2020).
7. P. Emsley, B. Lohkamp, W.G. Scott, K. Cowtan, Features and development of Coot. *Acta Crystallogr D Biol Crystallogr* **66**, 486-501 (2010).
8. P.V. Afonine *et al.*, Real-space refinement in PHENIX for cryo-EM and crystallography. *Acta Crystallogr D Struct Biol* **74**, 531-544 (2018).
9. D. Liebschner *et al.*, Macromolecular structure determination using X-rays, neutrons and electrons: recent developments in Phenix. *Acta Crystallogr D Struct Biol* **75**, 861-877 (2019).
10. T.D. Goddard *et al.*, UCSF ChimeraX: Meeting modern challenges in visualization and analysis. *Protein Sci* **27**, 14-25 (2018).
11. J. Gu *et al.*, Cryo-EM structure of the mammalian ATP synthase tetramer bound with inhibitory protein IF_1. *Science* **364**, 1068-1075 (2019).
12. F. Madeira *et al.*, The EMBL-EBI search and sequence analysis tools APIs in 2019. *Nucleic Acids Res.* **47**, W636-W641 (2019).
13. D.T. Jones, Protein secondary structure prediction based on position-specific scoring matrices 1 1Edited by G. Von Heijne. *J. Mol. Biol.* **292**, 195-202 (1999).
14. D.W.A. Buchan, D.T. Jones, The PSIPRED Protein Analysis Workbench: 20 years on. *Nucleic Acids Res.* **47**, W402-W407 (2019).
15. D.W. Buchan, F. Minneci, T.C. Nugent, K. Bryson, D.T. Jones, Scalable web services for the PSIPRED Protein Analysis Workbench. *Nucleic Acids Res.* **41**, W349-57 (2013).